Astronomy
&
Astrophysics

2MASS wide field extinction maps

I. The Pipe nebula

M. Lombardi[1,2], J. Alves[1], and C. J. Lada[3]

[1] European Southern Observatory, Karl-Schwarzschild-Straße 2, 85748 Garching bei München, Germany
 e-mail: mlombard@eso.org
[2] University of Milan, Department of Physics, via Celoria 16, 20133 Milan, Italy
[3] Harvard-Smithsonian Center for Astrophysics, Mail Stop 42, 60 Garden Street, Cambridge, MA 02138, USA

ABSTRACT

Aims. We present a $8° \times 6°$, high resolution extinction map of the Pipe nebula using 4.5 million stars from the Two Micron All Sky Survey (2MASS) point source catalog.

Methods. The use of NICER (Lombardi & Alves 2001, A&A, 377, 1023), a robust and optimal technique to map the dust column density, allows us to detect a $A_V = 0.5$ mag extinction at a 3-σ level with a 1 arcmin resolution.

Results. (*i*) We find for the Pipe nebula a *normal* reddening law, $E(J - H) = (1.85 \pm 0.15)E(H - K)$. (*ii*) We measure the cloud distance using Hipparchos and Tycho parallaxes, and obtain 130^{+24}_{-58} pc. This, together with the total estimated mass, $10^4\ M_\odot$, makes the Pipe the closest massive cloud complex to Earth. (*iii*) We compare the NICER extinction map to the NANTEN ^{12}CO observations and derive with unprecedented accuracy the relationship between the near-infrared extinction and the ^{12}CO column density and hence (indirectly) the ^{12}CO X-factor, that we estimate to be 2.91×10^{20} cm^{-2} K^{-1} km^{-1} s in the range $A_V \in [0.9, 5.4]$ mag. (*iv*) We identify approximately 1500 OH/IR stars located within the Galactic bulge in the direction of the Pipe field. This represents a significant increase of the known numbers of such stars in the Galaxy.

Conclusions. Our analysis confirms the power and simplicity of the color excess technique to study molecular clouds. The comparison with the NANTEN ^{12}CO data corroborates the insensitivity of CO observations to low column densities (up to approximately 2 mag in A_V), and shows also an irreducible uncertainty in the dust-CO correlation of about 1 mag of visual extinction.

Key words. ISM: clouds – ISM: dust, extinction – ISM: structure – ISM: individual objects: Pipe molecular complex – methods: data analysis

1. Introduction

Nearby Galactic molecular clouds complexes represent our best chance to understand cloud formation and evolution and hence to learn how stars come to be. But progress on the study of these objects has been slow. Not only are molecular clouds the coldest objects known in the Universe, their main mass component (H_2) cannot be detected directly. Most of all we know today about their physical properties has been derived through radio spectroscopy of H_2 surrogate molecules (CO, CS, NH_3; e.g., Blitz & Williams 1999; Myers 1999) and more recently through thermal emission of the dust grains inside these clouds (Andre et al. 2000; Johnstone et al. 2000). The results obtained using these techniques, especially the estimate of column densities, are not always straightforward to interpret and are plagued by several poorly constrained effects. Moreover, although large scale maps of entire molecular cloud complexes are now available (Heyer et al. 1998; Simon et al. 2001), maps with sufficient resolution and dynamic range to identify not only dense molecular cores but also their extended environment are still not existent. This wide view on molecular clouds is at present an obvious gap in our understanding of the relation between the dense Interstellar Medium (ISM) and star formation.

A straightforward and powerful technique to study molecular cloud structures, pioneered by Lada et al. (1994) and known as the Near-Infrared Color Excess method (NICE, Alves et al. 1998)

makes use of the most reliable tracer of H_2 in these clouds: extinction by pervasive dust grains in the gas. The NICE method relies on near-infrared (NIR) measurements of extinguished background starlight to derive accurate line-of-sight estimates of dust column densities. Depending on the stellar richness and color properties of the background field this technique can produce column density maps with spatial resolutions down to 5 arcsec (e.g. Alves et al. 2001, 2002) and with dynamic ranges more then an order of magnitude larger than classical optical star count techniques. This novel view on molecular clouds is providing not only new information on the physical structure of these object (Alves et al. 2001) but also an insight into their chemical structure and the physical properties of the dust grains, when combined to molecular line and dust emission data (Kramer et al. 1998, 1999; Alves et al. 1999; Bergin et al. 2001; Lada et al. 2003; Bianchi et al. 2003; Kramer et al. 2003).

In part to make use of the wealth of NIR data provided by the Two Micron All Sky Survey (2MASS, Kleinmann et al. 1994) the NICE method was further developed into an optimized multi-band technique dubbed Near-Infrared Color Excess Revisited (NICER, Lombardi & Alves 2001, hereafter Paper I). This generalization of NICE can, nevertheless, be applied to any multi-band survey of molecular clouds. Through use of optimal combinations of colors, NICER improves the noise variance of a map by a factor of two when compared to NICE. This unique property of NICER makes it the ideal tool to trace large scale

distributions of low column density molecular cloud material. When applied to 2MASS data, Nicer dust extinction maps trace not only the low column density regions ($A_V \simeq 0.5$ mag) but have the dynamic range to identify dense molecular cores by reaching cloud depths of ~30 mag of extinction, corresponding to 8×10^{22} protons cm^{-2} (Lombardi 2005).

In this paper we present an extinction map of the Pipe nebula covering 48 sq deg, computed by applying the Nicer technique on 4.5 millions *JHK* photometric measurements of stars from the 2MASS database. The Pipe nebula is a poorly studied nearby complex of molecular clouds. The only systematic analysis of this region is the one of Onishi et al. (1999) who present a ~27 sq deg map in the $J = 1-0$ line of ^{12}CO observed on a 4 arcmin grid, and smaller maps of selected regions in the $J = 1-0$ lines of ^{13}CO and C^{18}O. They estimate the total ^{12}CO mass to be ~10^4 $M_\odot$ (for a cloud distance of 160 pc) and point out that star formation is only occurring on Barnard 59, where the C^{18}O column density is the highest and where they find a CO outflow. Barnard 59 was also observed at 1300 μm by Reipurth et al. (1996) and a protostellar candidate B59-MMS1 was found. Two pre-main sequence stars associated with Barnard 59 appear in the young binaries survey of Reipurth & Zinnecker (1993) and more recently in Koresko (2002).

This paper is organized as follows. In Sect. 2 we describe the technique used to map the dust in the Pipe nebula and we present the main results obtained. In Sect. 3 we address the determination of the cloud distance using Hipparcos data. A statistical analysis and a discussion of the bias introduced by foreground stars is presented in Sect. 4. We compare the CO observations from Onishi et al. (1999) with our outcome in Sect. 5. Section 6 is devoted to the mass estimate of the cloud complex. Finally, we summarize the conclusions of this paper in Sect. 7.

In the following we will normally express column densities in terms of the 2MASS K_s band extinction A_K. When converting this quantity into the widely used visual extinction A_V, we will use the Rieke & Lebofsky (1985) reddening law converted into the 2MASS photometric system (see Carpenter 2001), $A_K/A_V = 0.112$.

2. Nicer extinction map

The data analysis was carried out using the Nicer method described in Paper I (to which we refer for more detailed information). Infrared J (1.25 μm), H (1.65 μm), and K_s band (2.17 μm) magnitudes of stars in the Pipe region were obtained from the Two Micron All Sky Survey[1] (2MASS, Kleinmann et al. 1994). We selected a large region around the Pipe nebula, characterized by galactic coordinates

$$-4° < l < +4°, \qquad +2° < b < +8°. \qquad (1)$$

As shown by these coordinate ranges, the Pipe nebula occupies an exceptionally good location for infrared studies. Indeed, this cloud complex is just above the galactic plane and is in front of the galactic bulge (see Fig. 1). The cloud, we anticipate, is approximately at 130 pc (see Sect. 3), and thus almost all the stars observed in direction of the cloud are background objects. As a result, we could carry out the study of the infrared extinction of the cloud with negligible contamination by foreground objects (except in the most dense regions).

The high density of stars in the Pipe region has also some drawbacks. Indeed, because of confusion, the nominal 2MASS

Fig. 1. Color optical image of the region around the Pipe nebula. The bright "star" on the top-right is Jupiter; below it are well visible the ρ-Ophiuci dark cloud and the Lupus complex. The white box encloses the field studied in this paper. The Pipe nebula obscures part of the Galactic bulge, and thus occupies an exceptional location for infrared studies (image courtesy Jerry Lodriguss, http://www.astropix.com/).

photometric completeness limits drop close to the galactic center. In the case of Nicer (in contrast with the star-counting method), this does not affect the measurements of column densities because no assumptions are made about the local star density. High density regions also pose severe challenges for data reduction. For example, the pipeline used for the Second Incremental Release of 2MASS produced slightly inaccurate zero-points. This problem showed on the Nicer maps of the Pipe nebula as abrupt artificial changes in the measured column density at the boundaries of the 2MASS observation tiles. Fortunately, the pipeline has been greatly improved and this problem does not appear in the final 2MASS All Sky Release.

After selecting point sources from the 2MASS catalog inside the boundaries (1), we generated a preliminary extinction map. As described in Paper I, this map was mainly used as a first check of the data, to select a control region on the field, and to obtain there the photometric parameters to be used in the final map (see Fig. 7). We note that the search of a control field close to the Pipe nebula has been non-trivial, because of the complex cloud structure and high column densities observed at low galactic latitudes. We identified in the Eastern part of our field (top-right in Fig. 7) a small region that is apparently affected by only a negligible extinction (see below); note that the newly determined Indebetouw et al. (2005) 2MASS reddening law was used at this stage.

Using the information provided by the control field, we generated a second map, which is thus "calibrated" (i.e., provides already, for each position in our field, a reliable estimate of the column density). We then considered the color−color diagram for the stars in the catalog. The result, shown in Fig. 2, shows a surprising bifurcation for $H − K > 1$ mag, which in principle might represent a problem in color-excess studies.

In order to further investigate the origin of this bifurcation, we considered the region $H − K > 1$ mag in the color−color diagram, and divided it into two subsamples *A* (upper branch) and *B* (lower branch) according to the expressions
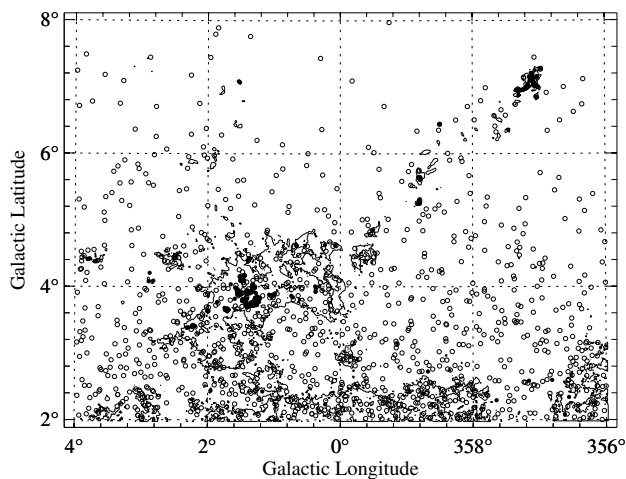
$$A \equiv \{1.4(H − K) + 0.5 \text{ mag} < (J − H)\}, \qquad (2)$$
$$B \equiv \{1.4(H − K) + 0.5 \text{ mag} > (J − H)\}. \qquad (3)$$
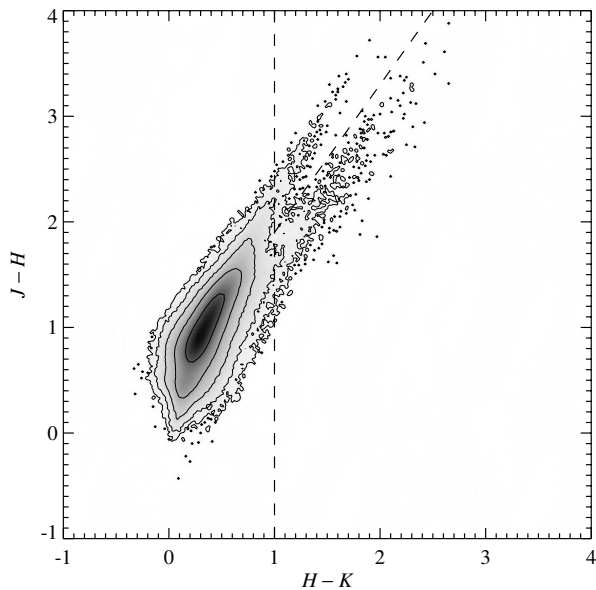
Fig. 2. Color−color diagram of the stars in the Pipe nebula field, as a density plot. The contours are logarithmically spaced, i.e. each contours represents a density ten times larger than the enclosing contour; the outer contour detects single stars and clearly shows a bifurcation at large color-excesses.


Fig. 3. Spatial distribution of the subsample of sources as defined by Eqs. (2) and (3). Subsample A is shown as filled circles, while subsample B is shown as open circles (see also Fig. 2). Subsample A appears to be strongly clustered in high-column density regions of the cloud, and are thus interpreted as genuine reddened stars; subsample B seems not to be associated with the cloud, and are instead preferentially located at low galactic latitudes. The contour line represents the $A_K = 0.6$ contour of the Pipe nebula.

We then analysed the spatial distribution of the stars contained in the two regions. The results, shown in Fig. 3, give a first strong indication that, as expected from their location in the color−color diagram, subsample A is associated with the densest regions of the molecular cloud and thus it has to be interpreted as normal stars reddened by the dust, while subsample B does not appear to be associated with the cloud. Interestingly, subsample B is uniformly distributed in galactic longitude, but has a strong preference for low galactic latitude regions.

Further hints on the nature of the two stellar populations in subsamples A and B are given by the histogram of their K band magnitudes, shown in Fig. 4. Interestingly, while
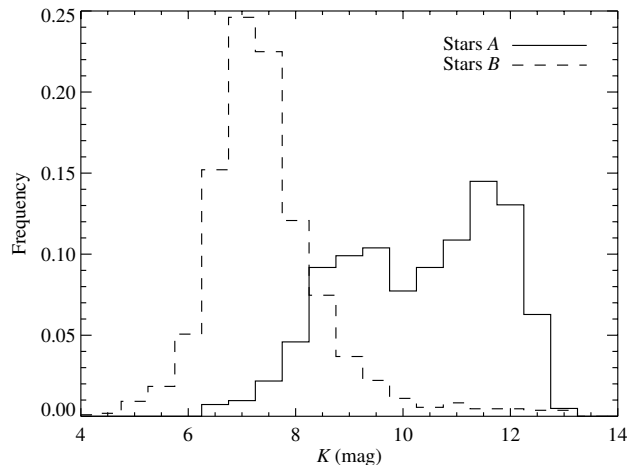
Fig. 4. The histogram of the K band magnitude for the two star subsets A and B of Eqs. (2) and (3).
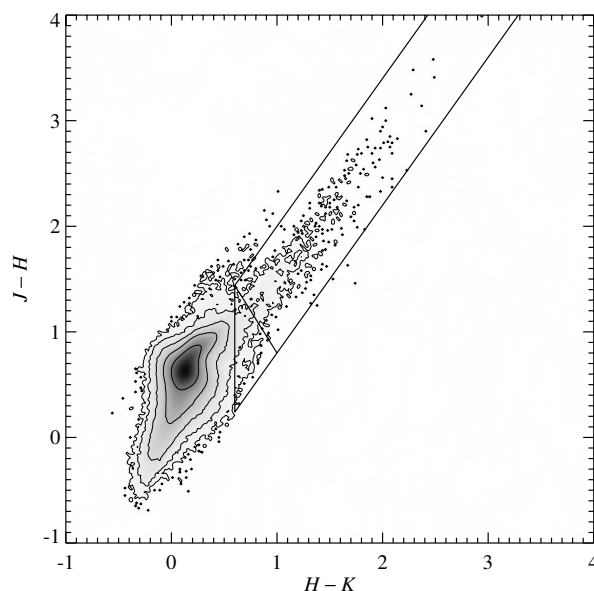
Fig. 5. The extinction-corrected color−color diagram for the Pipe nebula. The stripes show both subsamples B_1 and $B_2 \subset B_1$ (cf. Eqs. (4) and (5)).

subsample A stars show, as expected, a broad distribution, with number counts increasing at relatively large magnitudes, the B stars show a well defined distribution, with a strong peak at $K \simeq 7$ mag.

The lack of correlation between the dust reddening and the stars of subsample B is also well expressed by extinction-corrected color−color diagram, shown in Fig. 5. This plot has been constructed by estimating, for each star of Fig. 2, its *intrinsic* color, obtained by correcting the observed one by the measured NICER extinction at the location of the star (cf. Fig. 7). This analysis, based on the simplifying assumptions that all stars are background to the molecular cloud and that the extinction is basically constant on the resolution of our map, is however able to capture the essential characteristics of the distribution of *intrinsic* star colors. By comparing Fig. 5 with Fig. 2, in particular, we see that the upper branch, subsample A, essentially disappears in the extinction-corrected plot, while the lower branch, subsample B, is largely left unchanged. Because of the much shrunken distribution of stars, Fig. 5 is particularly useful to better identify

stars belonging to the lower branch. We defined thus in this plot two sets

$$B_1 \equiv \left\{ \left| 1.4(H - K)_{\text{intr}} - (J - H)_{\text{intr}} \right| < 0.6 \right.$$
$$\left. \text{and } (H - K)_{\text{intr}} > 0.6 \right\}, \tag{4}$$

$$B_2 \equiv \left\{ \left| 1.4(H - K)_{\text{intr}} - (J - H)_{\text{intr}} \right| < 0.6 \right.$$
$$\left. \text{and } (J - H)_{\text{intr}} > -1.6(H - K)_{\text{intr}} + 2.4 \right\}. \tag{5}$$

Note that $B_2 \subset B_1$. These two sets, marked in Fig. 5, correspond to the areas in the color–color plot where a contamination by subsample B stars is possible (B_1), or highly likely (B_2).

From the elements considered so far, we can carry out the following conclusions with respect to the nature of the B subsample that from this point on will be called the "lower branch":

- These stars are unrelated to the molecular cloud reddening and appear to be located close to the galactic plane. A deeper analysis, carried out on a much larger field (Lombardi et al., in prep.), actually shows that the stars are preferentially located on the galactic bulge.
- The stars occupy a well defined region in the (extinction-corrected) color–color diagram. This indicates that the "lower branch" represents a well-defined population of stars.
- The K band distribution of "lower branch" stars is strongly peaked at $K \simeq 7$ mag. This not only is a further indication that we are looking at a homogeneous population, but also suggests that these stars are at essentially the same *distance*. The K-band standard deviation is approximately 0.8 mag (if the tail at $K > 10$ mag of Fig. 4 is neglected), and since this must account for the scatter in the absolute magnitude, the scatter in the distance, and the photometric errors, it is likely that these stars have a relative scatter in their distance of the order of 25% or less. Again, this is a further hint that the "lower branch" stars might be a bulge population.
- The distribution of "lower branch" stars in the color–color diagram (Fig. 2) forms an elongated region parallel to reddening vector. This shows that at least part of the large scatter in their intrinsic colors might be due to reddening, local or along the line of sight.

The items above suggest that the "lower branch" might be populated by evolved intermediate mass stars (about 1 to 7 $M_\odot$), and likely on the Asymptotic Giant Branch (AGB), at about the distance to the Galactic center. We find a similarity between the "lower branch" stars and the sample of Galactic OH/IR stars in Jiménez-Esteban et al. (2005). These authors conclude that the luminosity and color distribution observed could be explained as the result of a combined emission of a cool star ($T \sim 2500$ K) and a much cooler dust shell ($T < 800$ K). The main effect of the shell in the near-infrared colors would be to increase the circumstellar reddening, which, together with differential interstellar extinction effects from source to source, could explain the width of the distribution observed. Although we will not explore further in this paper the nature of these stars we note that they are particularly interesting objects, and given the large number of identifications in our fields (we have approximately 45 000 B_1 stars and 1500 B_2 ones) a dedicated study is warranted.

The "lower branch" stars seem to be unrelated to the molecular cloud, but their colors would be interpreted by the NICER algorithm as a sign of extinction. This, clearly, could in principle bias our results toward a higher extinction, especially at low galactic latitude regions. However, we argue that the bias introduced by "lower branch" stars is negligible. Indeed, the density of these objects is, in the worse case (set B_1) only 1% of
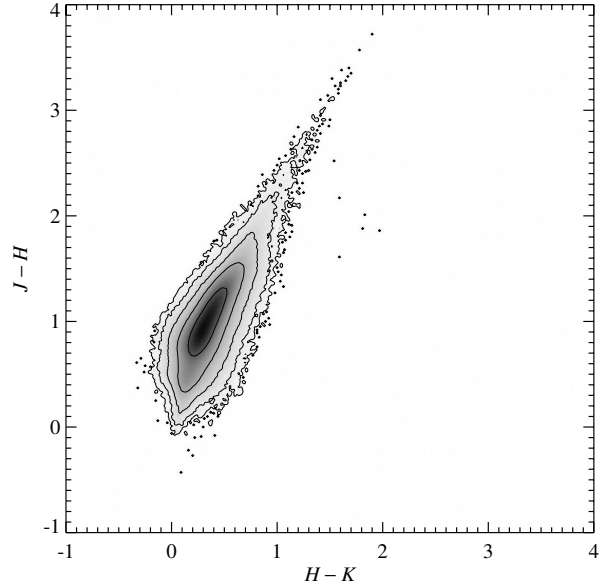

Fig. 6. The color–color diagram for the selected stars in the field, after the removal of the set B_2 of Eq. (5). A comparison with Fig. 2 shows that we were able to virtually remove all significant contamination from spurious reddening.

the average density of stars, so that typically we have at most one "lower branch" star contaminating each pixel, and since we have ~30 stars per pixel, the effects of "lower branch" stars is negligible everywhere.

Nevertheless, and in order to avoid any source of bias, although small, we excluded from the 2MASS catalogs all stars located in the B_2 color-space region, and performed the whole analysis described in this paper using this reduced subset of stars. We stress that if we had performed a a cut in the *observed* colors, we would be have introduced a new bias in the deduced column density; instead, the use of a select in the *intrinsic* colors does not bias the final results. As an example, Fig. 6 shows the color–color diagram for the new set of stars: note that the "lower branch" disappears completely in this plot, a further confirmation that our selection is effective in removing this population of stars.

We then run again the whole NICER pipeline on the refined catalog. After (re)evaluating the statistical properties of stars in the control field, we constructed the final map, shown in Fig. 7, in a grid of approximately 1000×750 points, with scale 30 arcsec per pixel, and with Gaussian smoothing characterized by *FWHM* $= 1$ arcmin; moreover, we used an iterative σ-clipping at 3-σ error. The final, *effective* density of stars is ~8 stars per pixel (this value changes significantly on the field with the galactic latitude, see Fig. 8); this guarantees an average (1-σ) error on A_K of only 0.019 mag; the largest extinction is measured close to Barnard 59, where $A_K \simeq 2.68$ mag (corresponding to approximately $A_V \simeq 24$ mag). As clearly shown by Fig. 7, the combination of the use of the 2MASS archive with the optimized NICER technique allows us to reveal an unprecedented number of details. A quantitative analysis of this extinction map is delayed until Sect. 4.

Figure 9 shows the expected error on A_K for each pixel of the extinction map. This figure deserves a few comments. First, we note that the most significant variations in the expected error are due to bright stars, which produce the characteristic cross-shaped patterns (cf. Fig. 8). We observe that, with the help of Fig. 9, some apparent features in the extinction map are actually
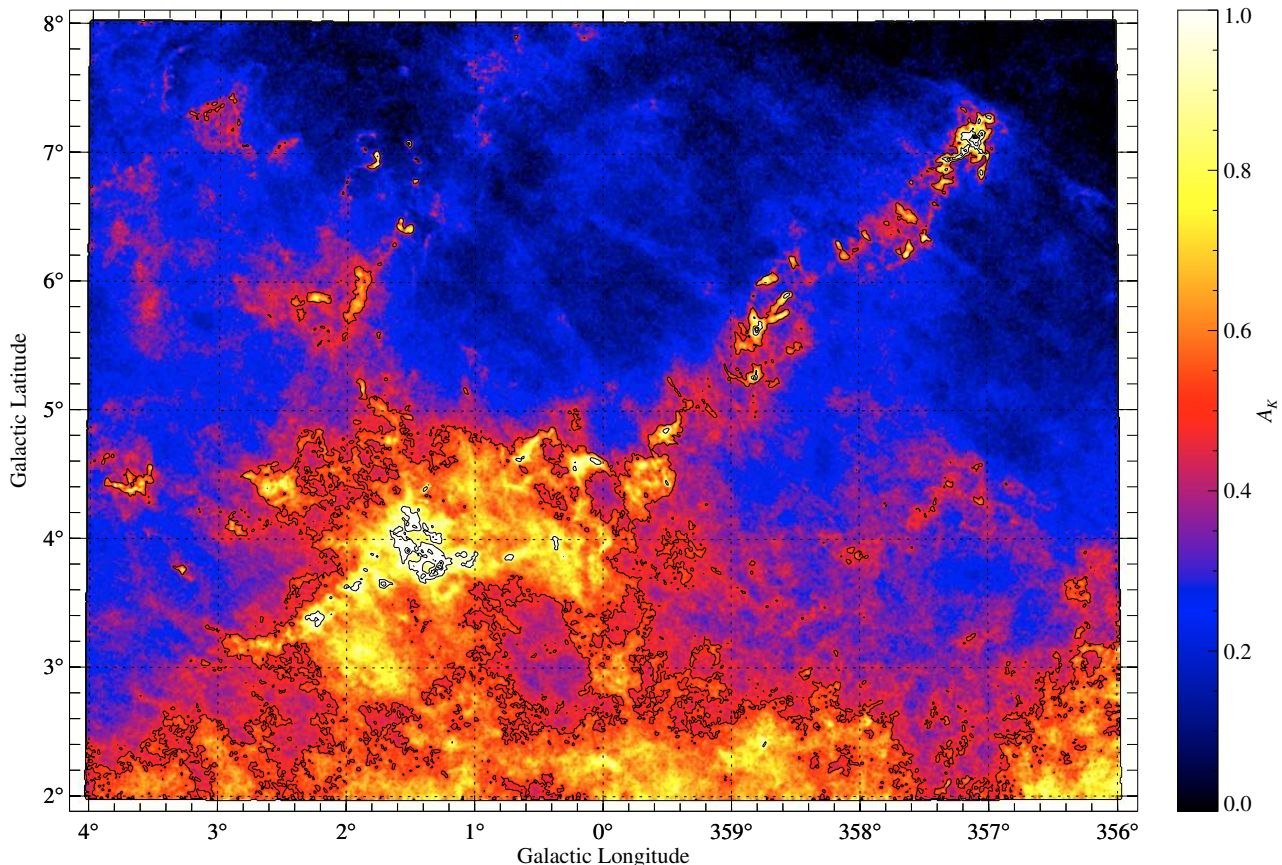
Fig. 7. The NICER extinction map of the Pipe nebula. The resolution is *FWHM* = 1 arcmin; the contours are at $A_K = \{0.5, 1, 1.5\}$ mag.

recognized to be due to the larger noise expected close to bright stars (these "features", hence, are just increased statistical deviations due to the increased local error). This clearly shows that a detailed analysis of the extinction map of Fig. 7 is better carried out using also the density map of Fig. 8 and the error map of Fig. 9. Figure 9 shows also an increase in noise in the densest regions of the cloud, due to the reduced density of background stars. Finally, we note the increase of the error with the galactic latitude, also due to a change in the density of background stars.

The accuracy of the column density measurements obtained in our field is shown by Fig. 10, which plots the expected error on A_K as a function of A_K for all pixels in our field. The exquisite data used allowed us to keep the average error well below 0.02 mag in A_K, and still to have a 1 arcmin resolution in our maps. The dynamical range of the NICER extinction map can be better appreciated by noting that the lowest contour in Fig. 7 represents a $\sim 10\sigma$ detection, and that clumps such as Barnard 59 have a significance as large as $\sim 200\sigma$. Note that the increase on the error observed for $A_K < 0.2$ mag in Fig. 10 is due to the fact that regions with low extinction (including the control field) are located at high galactic latitudes, and hence have a smaller density of background stars.

3. Distance

An accurate determination of the distance of molecular clouds is of vital importance to obtain a reliable estimate of the mass and of other physical properties. Unfortunately, distance measurements of molecular clouds are frequently plagued by very large uncertainties. A simple method used often is based on the association between the cloud and other astronomical objects whose

distance is well known. Onishi et al. (1999) associate the Pipe nebula with the Ophiuchus complex on the base of projected proximity and radial velocity and use the distance of the latter, (160 ± 20) pc, as the distance to the Pipe (Chini 1981).

An alternative approach is based on the number counts of foreground stars. The method, used for example in Alves et al. (1998), exploits the large reddening produced by some clouds, which makes the identification of foreground stars relatively easy; then, galactic models (e.g. Bahcall & Soneira 1980; Wainscoat et al. 1992) are used to infer the expected number of stars (for each possible cloud distance) inside the cone created by the cloud. Finally, the number of foreground stars observed is compared to the prediction and the distance of the cloud is inferred. Although this method is often the best one can use, it is unable to give accurate distances for several reasons: (i) it relies on galactic models, which might be inaccurate (especially at the small angular scales often used for molecular clouds); (ii) it is plagued by Poisson noise (because the number of stars inside the volume of the cone is a random variable) and (iii) stars do cluster (and thus the error is actually larger than the one expected from a Poisson statistics; imagine, in the extreme, the case of an unknown open cluster in front of the cloud).

A more robust determination of the distance of the Pipe molecular complex can be obtained using the Hipparcos and Tycho catalogs (Perryman et al. 1997). The method, similarly to the star number counts described in the previous section, is based on the identification of foreground and background stars (observed on the line of sight of the cloud) for which a parallax estimate is available. An upper limit for the distance of the cloud is thus given by the distance of the closest background star, i.e. the closest star showing a significant extinction in its colors. This
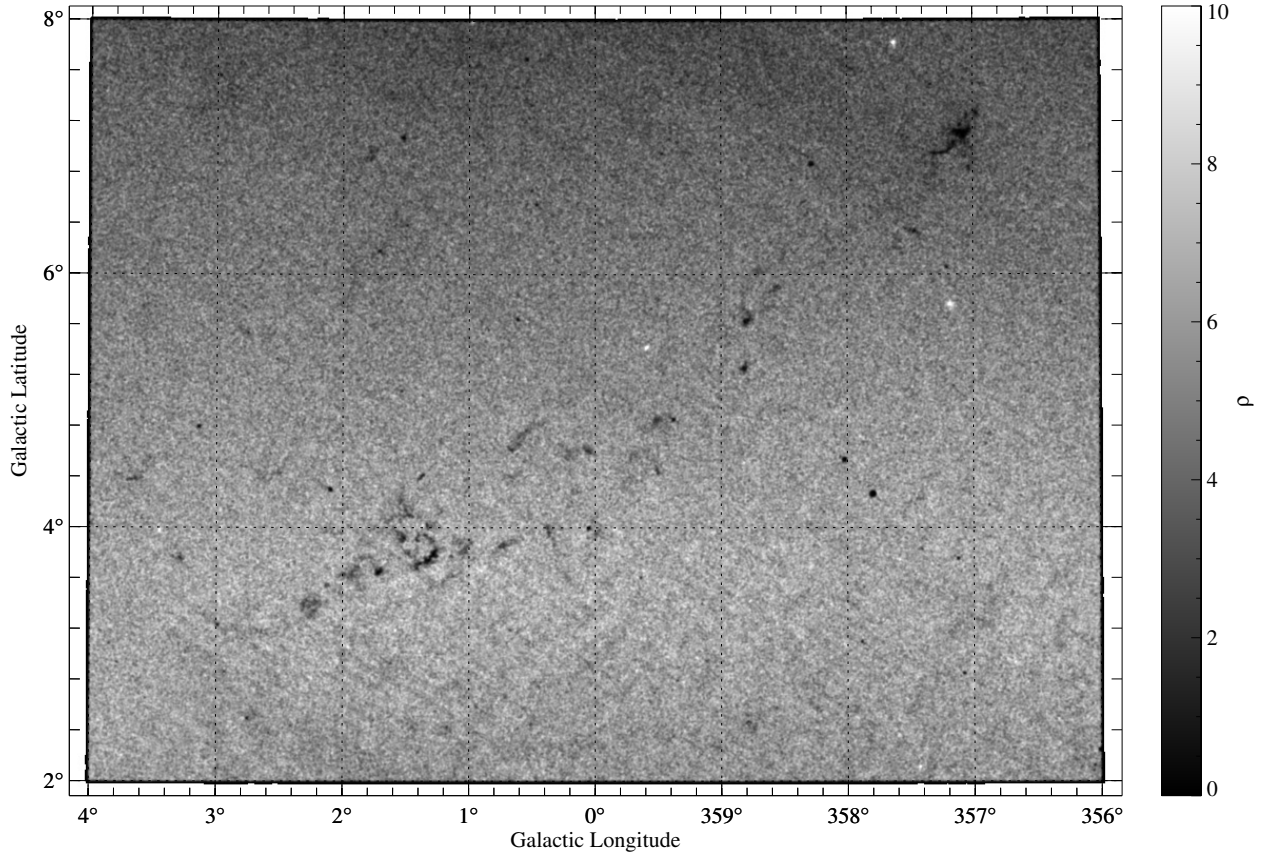
Fig. 8. The star density map for the extinction map of Fig. 7, i.e. the number of stars inside a (Gaussian) 1 arcmin beam. The dark structures correspond mostly to the position of dense cores in the Pipe nebula where the star density in minimal due to high extinction. The black "holes" outside the Pipe body correspond to masked bright stars while the white spots correspond to globular clusters.

novel approach to the distance of molecular cloud complexes has already been successfully applied to several clouds by Knude & Hog (1998). Here we revisit the method and use it to obtain a distance estimate for the Pipe nebula.

We selected Hipparcos and Tycho-1 (I/239) stars observed in the area defined in Eq. (1), and matched these stars with the "All-sky Compiled Catalog of 2.5 million stars" (ASCC-2.5, I/280A; Kharchenko 2001) and with the "Tycho-2 Spectra Type Catalog" (Tycho-2spec, III/231; Wright et al. 2003). The choice of these two latter datasets (which are cross-references and merges of many stellar catalogs) was dictated by the need to obtain for each star with measured parallax an estimate of its spectral type. In particular, the use of ASCC-2.5 and of Tycho-2spec effectively allowed us to cover a large sample of spectroscopic catalogs: the Hipparcos catalog (I/239), the Carlsberg Meridian Catalogs (CMC11; I/256), the Position and Proper Motions (PPM; I/146, I/193, I/208), the Michigan Catalogs (III/31, III/51, III/80, III/133, III/214), the Catalog of Stellar Spectra Classified in the Morgan-Keenan System (III/18), the MK Classification Extension (III/78), and the FK5 catalog parts I and II (I/149 and I/175).

We considered all stars in our field with measured parallax larger than the parallax error, and with spectral type B, A, F, G, K, or M. By comparing the expected $B - V$ color (taken from Landolt-Börnstein 1982, p. 15) with the observed one, we obtained an estimated of the color excess $E(B - V)$; we finally converted this into an extinction in the V band A_V by using a normal reddening law, $A_V = 3.09E(B - V)$ (Rieke & Lebofsky 1985). Note that, whenever possible, we used 2D spectral types; for 1D spectral types we assumed a luminosity class IV.

A plot of the star column density versus the Hipparcos and Tycho2 parallaxes is shown in Fig. 11. Because of the relative large scatters in the parallax and column density measurements, Fig. 11 is not straightforward to interpret. However, we note the following points.

1. At large parallaxes, for $\pi > 12$ mas, the measured extinction is low and consistent, within the errors, with a constant value. The average extinction in this range, $\langle A_V \rangle = 0.12$ mag, either suggests the presence of a thin "veil" very close to us or of a small systematic error in the estimate of A_V. The presence of absorbing material towards the location of the Pipe nebula at distances below 50 pc is also suggested by the recent work of Lallement et al. (2003), where they construct 3D absorption maps of the local distribution of neutral gas through measurements of equivalent widths of the interstellar NaI D-line doublet towards nearby stars. In any case, from Fig. 11 we can deduce a robust lower limit on the cloud distance, $d > 80$ pc. Note that, interestingly, we also detect a near single star (HD 158233) at (55.0 ± 1.67) mas with significant reddening, $A_V = (0.38 \pm 0.06)$ mag: thus, if the reddening has to be attributed to a thin molecular cloud, its distance would be smaller than 20 pc.
2. As we go to smaller parallaxes we start seeing stars with signs of a possible reddening. A first candidate is a star at 90 pc with $A_V = (1.11 \pm 0.66)$ mag (well visible in Fig. 11); however, the large error on A_V does not allow us to assess securely that the star has been significantly reddened by the cloud.
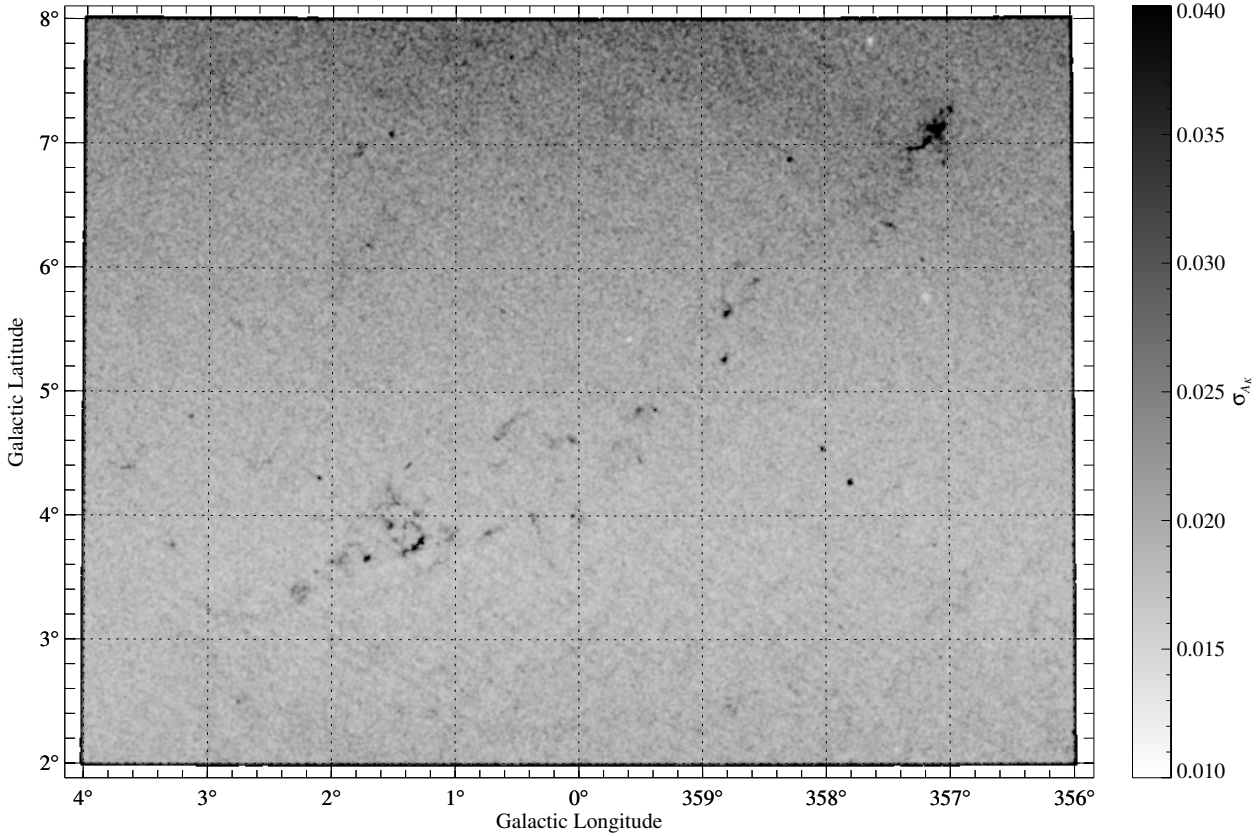
Fig. 9. The map shows the statistical error σ_{A_K} on the measured column density. Note that correlation on the errors on a scale of *FWHM* = 1 arcmin is expected. This map shows that for almost the whole field $A_K = 0.05$ represents a 3-σ detection.
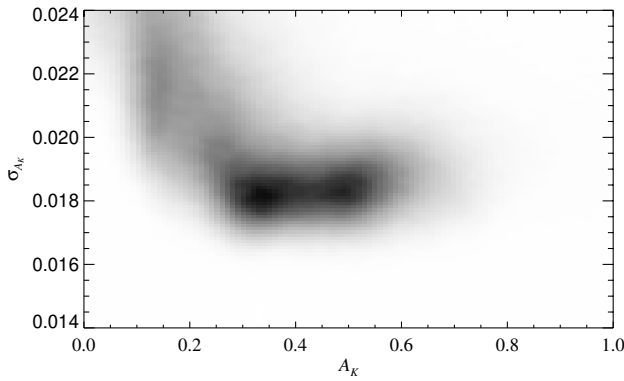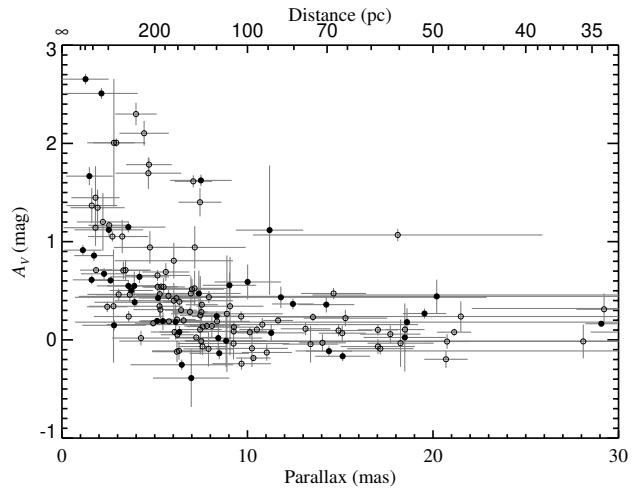

Fig. 10. The expected error σ_{A_K} versus the measured extinction A_K for the various pixels in the extinction map of Fig. 7, shown as a density plot.

Fig. 11. The reddening of Hipparcos and Tycho stars in the field. For this plot we selected only the stars characterized by a measured parallax $\hat{\pi}$ smaller than its error $\hat{\sigma}_\pi$, and have an estimated error on the column density $\hat{\sigma}_{A_V} < 1$ mag. Among the 151 stars that matches these constraints, we marked with a filled dots the 44 ones that are located at $b > 3°$.

3. At approximately $\pi = 7.3$ mas (∼137 pc) we observe four stars with relatively large extinction, $A_V > 0.9$ mag, and with relative small errors (the ratio A_V/Err(A_V) ranges from 4.3 to 27.5). Hence, these stars give an upper limit to the cloud distance, $d < 140$ pc.

In summary, the simple argument discussed above suggests that the Pipe nebula is located between 80 and 140 pc.

A more rigorous estimate of the distance can be obtained by using a statistical model for the parallax-extinction relation. The physical picture here suggests that we can take the star column density as a random variable whose distribution only depends on the intrinsic measurement errors and on the parallax of the star. The simplest sensible approach is to consider a bimodal distribution for each star column density, where the extinction of stars in front of the nebula is consistent (within the measurement errors) with zero, and the extinction of stars at distances larger than the cloud can be either still zero (if the star is not observed through the cloud) or finite and with a large scatter (if the star is behind the cloud). In this case, the conditional probability

of observing a star with visual extinction A_V given the fact that the star is located at a parallax π is

$$p(A_V \mid \pi) = \begin{cases} \mathrm{Gau}\left(A_V \mid A_V^{\mathrm{fg}}, \sigma_{A_V}^{\mathrm{fg2}} + \sigma_{A_V}^2\right) & \text{if } \pi > \pi_{\mathrm{Pipe}}, \\ (1-f)\mathrm{Gau}\left(A_V \mid A_V^{\mathrm{fg}}, \sigma_{A_V}^{\mathrm{fg2}} + \sigma_{A_V}^2\right) \\ \quad + f\mathrm{Gau}\left(A_V \mid A_V^{\mathrm{bg}}, \sigma_{A_V}^{\mathrm{bg2}} + \sigma_{A_V}^2\right) & \text{if } \pi \leq \pi_{\mathrm{Pipe}}, \end{cases} \quad (6)$$

where we denoted with $\mathrm{Gau}(x|\bar{x}, \sigma_x)$ the value at x of a normal probability density with mean $\bar{x}$ and variance σ_x^2 (cf. Eq. (12)). In other words, we use a normal distribution with low average A_V^{fg} for foreground stars, and the *mixture* of the same distribution with another normal (with large average A_V^{bg}) for background stars. For both distributions the variance was set to the sum of $\sigma_{A_V}^2$, the estimated variance in the measured column density of the star, and $\sigma_{A_V}^{\mathrm{fg2}}$ (respectively, $\sigma_{A_V}^{\mathrm{bg2}}$), the intrinsic variance of the foreground (background) distributions. The parameter $f \in [0, 1]$ used in Eq. (6) represents the *filling factor*, i.e. the ratio between the area of the sky occupied by the cloud and the area of the whole field.

We considered this simple model leaving as free parameters $\left\{\pi_{\mathrm{Pipe}}, f, A_V^{\mathrm{bg}}, \sigma_{A_V}^{\mathrm{bg2}}\right\}$ (the average foreground A_V and its variance were deduced from the stars with measured parallax $\hat{\pi} > 12$ mas). In order to assess the goodness of a model, we computed the likelihood function, defined as

$$\mathcal{L} = \prod_{n=1}^{N} \int_0^\infty p\left(A_V^{(n)} \mid \pi\right) p\left(\pi \mid \hat{\pi}^{(n)}\right) \mathrm{d}\pi, \quad (7)$$

where the product is carried over all N observed stars with parallax, and where $p\left(\pi \mid \hat{\pi}^{(n)}\right)$ is the probability distribution that the n-th star with measured parallax $\hat{\pi}^{(n)}$ has a true parallax π. The integral in Eq. (7) takes into account the possibility that a star with a measured parallax $\hat{\pi} < \pi_{\mathrm{Pipe}}$ (or $\hat{\pi} > \pi_{\mathrm{Pipe}}$) is incorrectly taken as background (respectively, foreground) because of its large parallax error $\hat{\sigma}_\pi$. In our analysis, we used for $p\left(\pi \mid \hat{\pi}^{(n)}\right)$ a simple normal distribution with standard deviation equal to the formal error on the measured parallax $\hat{\sigma}_\pi^{(n)}$:

$$p\left(\hat{\pi} \mid \pi^{(n)}\right) = \mathrm{Gau}\left(\hat{\pi} \mid \pi^{(n)}, \hat{\sigma}_\pi^{(n)2}\right). \quad (8)$$

We note that this particular choice allows us to evaluate the integrals of Eq. (7) analytically in terms of the error function erf.

In order to study in detail the likelihood function (7) in its multidimensional parameter space we used Monte-Carlo Markov Chains (MCMC; see, e.g. Tanner 1991). The obtained results are summarized by Fig. 12, where we show the marginalized likelihood as a function of the cloud parallax π. As best estimate for the cloud distance we take the median of the distribution shown in Fig. 12, $d_{\mathrm{Pipe}} = 130$ pc; the formal 68% (respectively, 95%) confidence regions are [110, 143] pc and [72, 154] pc. Note that the best fit value obtained for the filling factor is $f = 0.42$, which compares well with the value directly measured in the map of Fig. 7 (41% of the area in our field has a measured extinction $A_V > 3$ mag).

In summary, in the rest of this paper we will use a estimate of the cloud distance 130^{+13}_{-20} pc. The formal error is relatively small, but it is probably underestimated (e.g., the error due to a possible misclassification of the spectral type of a star was not included in the error budget); moreover, because of the relatively small number of reddened stars, the distance obtained appears to be slightly model-dependent. Our distance estimate is likely to
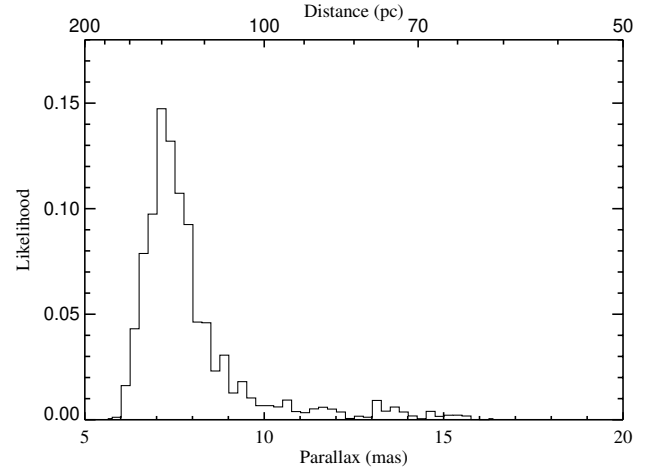
Fig. 12. The likelihood function of Eq. (7) as a function of the cloud parallax π_{Pipe} marginalized over all the other parameters. The function shows a marked peak at $\pi \simeq 7.13$ mas. The mean of π_{Pipe} is 8.07 mas, while the median is 7.61 mas, corresponding to a distance of approximately 130 pc.

be biased towards large values because the method used gives an *upper* limit (this is also suggested by the long tail at large parallaxes in the likelihood function of Fig. 12). With the advent of the new generation astrometric missions such as Gaia (Lindegren & Perryman 1996) it will be possible with this or similar methods to accurately measure the distances of a large sample of molecular cloud complexes.

4. Statistical analysis

4.1. Star extinction

In Fig. 13 we plot the distributions of column densities obtained for stars observed in low-extinction (-0.05 mag $< A_K <$ 0.05 mag) and high-extinction (1.15 mag $< A_K <$ 1.25 mag) regions. The two histograms show two similar Gaussian shapes, but the one corresponding to high-extinction has a larger width (the best-fit Gaussian dispersions are $\sigma_1 = 0.210$ mag and $\sigma_2 = 0.272$ mag). This increase can be due to a number of factors: (i) the increase of photometric errors for the faint stars observed through dense clouds, and the lack of the K band photometry for most of these objects; (ii) the internal structure of the cloud on scales smaller than our resolution (which, we recall, is FWHM = 1 arcmin); (iii) an increase in the contamination of foreground stars (see below Sect. 4.4). Among these factors, (i) can be evaluated from the photometric errors of the 2MASS database, and appears to negligible (i.e., there is no significant increase in the photometric error of stars in moderately extincted regions, cf. Fig. 10). On the other hand, factors (ii) and (iii) are difficult to disentangle, because they essentially produce the same effects (see below).

The increase of the dispersion on A_K at large column densities can be evaluated more quantitatively from Fig. 14. This figure has been obtained from the map of the dispersion of A_K (not shown here). This map is constructed by evaluating, for each pixel of Fig. 7, the scatter of the column density estimates corresponding to each star. Hence, large values in some pixels of this map mean that the stars used to estimate A_K in the corresponding pixels of Fig. 7 present very different reddening values (see Paper I for the analytic definition of the scatter map). Figure 14 has been obtained by plotting the average values observed in the
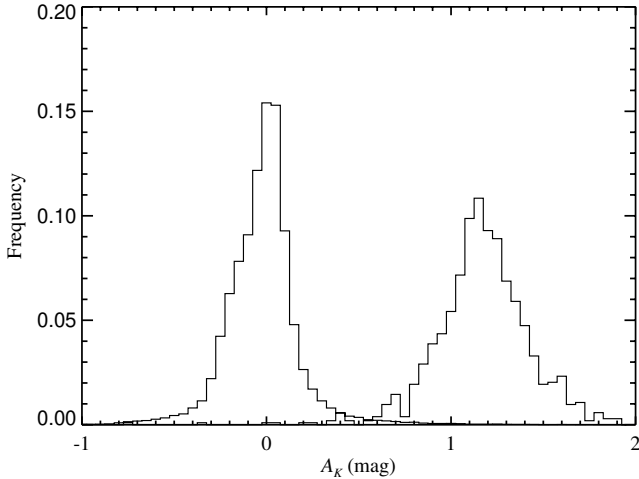
Fig. 13. The distribution of individual star extinctions. The solid histogram shows the distribution of column densities for stars observed in low-extinction regions ($-0.05 < A_K < 0.05$ on the extinction map); the dashed line the same distribution for stars in high-extinction regions ($1.15 < A_K < 1.25$).
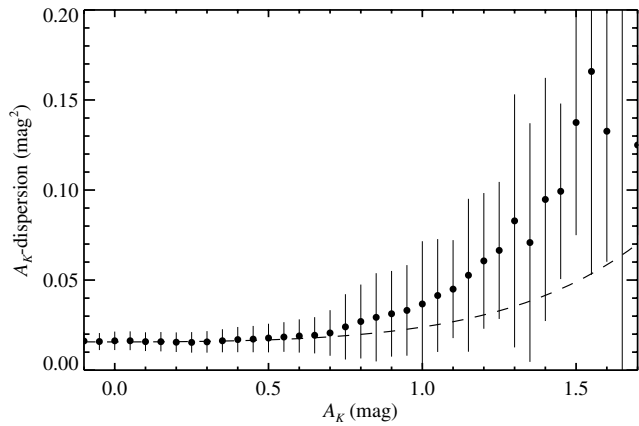
Fig. 14. The dispersion on the extinction measurements as a function of the column density A_K. In order to have a clear plot, we evaluated the dispersion on bins of 0.05 mag in A_K; the plot shows the average values obtained in each bin and the relative scatter. The dashed line represents the expected increase in the dispersion if we attribute this effect to the contamination of foreground stars.

dispersion map in pixels characterized by a given value of A_K in Fig. 7. We note that the observed increase in the dispersion of A_K has been observed in several similar studies (e.g. Lada et al. 1994; Alves et al. 1998; Lada et al. 1999).

As we mentioned above, in our case it is difficult to attribute the effect observed in Fig. 14 with certainty to foreground stars or to substructures. Consider, as an example, a "two-dimensional Swiss cheese" molecular cloud, i.e. a thin cloud with many holes (some of them smaller than the resolution of our maps). In this case, a background star observed through a small hole will produce exactly the same statistics as a foreground star. Hence, in this case it will be impossible to distinguish foreground stars and substructure. In less extreme (and more physical) situations it is generally possible to firmly identify, in the dense regions of the cloud complexes, foreground stars. However, this task is unfortunately non-trivial for the Pipe, because of its filamentary structure and of the relatively low resolution attainable with the 2MASS data. Still, our estimate indicates that only an extremely small fraction $F_0 \simeq 0.003$ of foreground stars is present in our

map (see below Sect. 4.4), and thus they have a negligible contribution to the effect observed in Fig. 14 (cf. dashed line in that figure). In summary, we attribute most of the increase in the dispersion of A_K to unresolved substructures. A further indication of this is given by similar analyses of molecular clouds carried out at a higher resolution (e.g. Lada et al. 2004), which show a dispersion σ_{A_V} substantially independent of A_K (i.e., a flat curve in the A_K-σ_{A_K} plot). In a follow-up paper (Lombardi 2005) we will further investigate the effect of substructures in molecular clouds.

4.2. Reddening law

The reddening law plays a fundamental role in any infrared dust measurement since it is used to derive the column dust density from the properties of background stars. In particular, a key assumption is that the reddening law is *linear*, i.e. that the ratio $A_{\lambda_1}/A_{\lambda_2}$ of extinctions in two different wavelengths is constant. Since the intrinsic luminosities of stars are not known, we cannot measure directly the extinction A_λ in a single band; in the NIR, however, we can measure with good accuracy the color excess $E(m_{\lambda_1} - m_{\lambda_2}) = A_{\lambda_1} - A_{\lambda_2}$, and this is the essence of the NICE and NICER techniques. Moreover, if we have good photometry in three bands, say J, H, and K, we can indirectly verify the assumption of a linear reddening law by checking that the color excesses $E(H - K)$ and $E(J - H)$ are linearly dependent. The large number of stars in the field allows us to perform this check with great accuracy.

The linearity of the reddening law, ultimately, is equivalent to say that the stars in the color−color plot are mostly found along a linear stripe, and the hypothesis is qualitatively well supported by Fig. 6. Still, this simple observation is not easily translated into a *robust* and *statistically accurate* method to measure the reddening law. This, in part, might be the origin of some discrepancies found in the literature about the slope of the reddening law (another good reason are the different NIR photometric systems used by different authors).

For example, in order to measure the slope of the reddening law, we can fit all star colors (or color excesses) with a linear relation:

$$(J - H) = \alpha(H - K) + \beta, \tag{9}$$

where $\alpha = (A_J - A_H)/(A_H - A_K)$ and β are taken to be constant for all stars. Naively, the fit could be done directly on the individual star colors $\{H_n - K_n\}$ and $\{J_n - H_n\}$, by minimizing the expression

$$\chi^2 = \sum_{n=1}^{N} \left[\alpha(H_n - K_n) + \beta - (J_n - H_n) \right]^2, \tag{10}$$

or similar expressions taking into account the photometric errors of stars. In reality, such a procedure leads to unsatisfactory results because the large majority of stars are subject to small or negligible reddening. In other words, a minimization of Eq. (10) would basically take into account only the lower-left part of the plot of Fig. 6, and would neglect the most interesting (highly reddened) stars (say, $H - K > 1$ mag).

In order to equally take into account all reddening regimes, we followed here a different procedure:

1. We evaluated the column density of each star by using the normal reddening law considered in this paper (Indebetouw et al. 2005).
2. We binned the stars according to their extinction in bins of 0.02 mag.

3. In each bin, we evaluated the average color excesses in $H-K$ and $J-H$, and the standard deviation in $J-H$. Note that the standard deviation in $J-H$ was calculated by referring all star colors inside the bin to the average $H-K$ color, or equivalently by evaluating the standard deviation of the expression

$$E(J-H)_{\text{corr}} = -\alpha\big[E(H-K) - \big\langle E(H-K)\big\rangle\big] \\ +E(J-H). \qquad (11)$$

This procedure ensures that the scatter in $E(J-H)_{\text{corr}}$ does not include the scatter due to the finite size of the bin in $K-H$.

4. We fitted all *positive* bins with a linear relationship of the form of Eq. (9) (in the fit we took into account the standard deviations evaluated in the previous point).

5. Finally, we repeated the whole procedure using the newly determined reddening law until convergence is achieved (which typically happens after two or three iterations).

The method presented above has many pleasant properties. First, all reddening regimes equally contribute to the fit, since by construction we equally use all bins of different column densities. This, in turn, implies that the method is robust against bright stellar populations that might artificially change the slope of the reddening law (cf. above Sect. 2). Moreover, the use of the *observed* standard deviations on the $J-H$ color for the fit properly takes into account local deviations from a reddening law or increased photometric errors for reddened stars.

We applied the method described above to our data, by selecting all 2MASS stars with accurate photometry in all bands (we required all photometric errors to be smaller than 0.1 mag) from the *cleaned* catalog (cf. above Sect. 2); the results obtained are summarized in Fig. 15. We found as best fit slope $\alpha = 1.82 \pm 0.03$, a value that appears to be in excellent agreement both the Indebetouw et al. (2005) 2MASS reddening law, $E(J-K)/E(H-K) = 1.78\pm0.15$, and with the Rieke & Lebofsky (1985) $E(J-K)/E(H-K) = 1.70$ normal reddening law converted into the 2MASS internal photometric system (Carpenter 2001), which is $E(J-K)_{2\text{MASS}}/E(H-K)_{2\text{MASS}} \simeq 1.89$.

In follow-up papers we will apply the same technique to other cloud complexes studied from the 2MASS archive. The uniformity of the 2MASS data and of the procedure used to derive the reddening law will allow us to accurately study cloud-to-cloud variations (see, e.g., Kenyon et al. 1998 for a case where significant differences from a standard reddening law are found).

4.3. Smoothing method

As discussed in Paper I, the pipeline developed allows us to obtain smooth maps of the discrete column density measurements (obtained for each background star) in three different ways: simple average, sigma-clipping, and median map. For the simple average we use all column density measurements close to each pixel, and the extinction value assigned to the pixel is a weighted average of the A_K measurements for each star. The weight takes into account both the statistical error on A_K (which is due to the photometric errors and to the intrinsic scatter of star colors), and the angular distance between the star and the pixel. For the sigma-clipping, instead, we selectively discard outliers on A_K, i.e. stars that have associated column densities significantly different from the local average. Finally, the median map is constructed by evaluating a sort of "weighted median" for the column densities measured for angularly close stars.

Figure 16 shows the relationship between the extinction measurements obtained through simple average and median. The
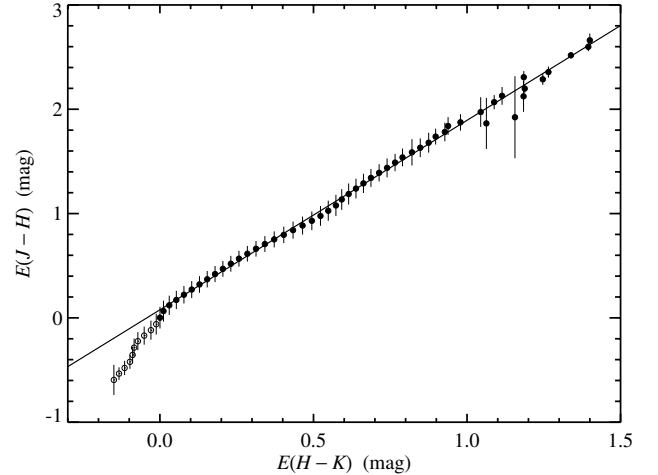

Fig. 15. The reddening law as measured on the analyzed region. The plot shows the color excess on $J-K$ as a function of the color excess on $H-K$ (the intrinsic colors, deduced from the control field, are 0.18 and 0.60 respectively); the solid line shows the best fit. Error bars represents the standard deviation of color excesses inside the bin.
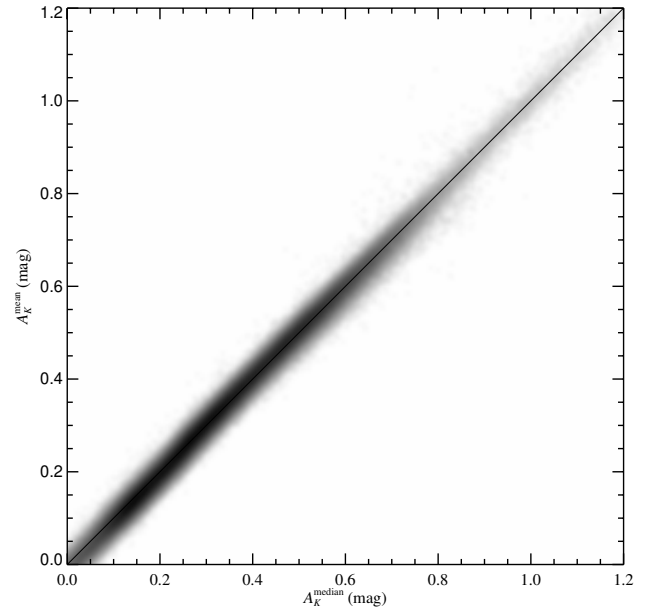

Fig. 16. Plot of the column densities for the various pixels of the extinction map obtained through median filter and simple average. The diagonal line shows the locus $A_K^{\text{median}} = A_K^{\text{mean}}$.

very tight band show that the two methods give comparable results. A more quantitative analysis is provided by Fig. 17, where an histogram of the differences between the simple mean and the median for each pixel is presented. Note that the two methods are statistically indistinguishable up to $A_K \simeq 1.5$ mag, where the mean starts to estimate consistently smaller column densities. Hence, this confirms that the use of the simple mean is justified up to relatively high column densities. Figure 17 also shows an increase in the scatter at high column densities, an indication of a difference in the extinction estimates at the corresponding sky locations using the mean and the median smoothing techniques. Unresolved structures in the cloud, which are expected in the dense regions, are the most probably reason for the observed scatter (substructures are likely to play different roles in the simple mean and median smoothing).
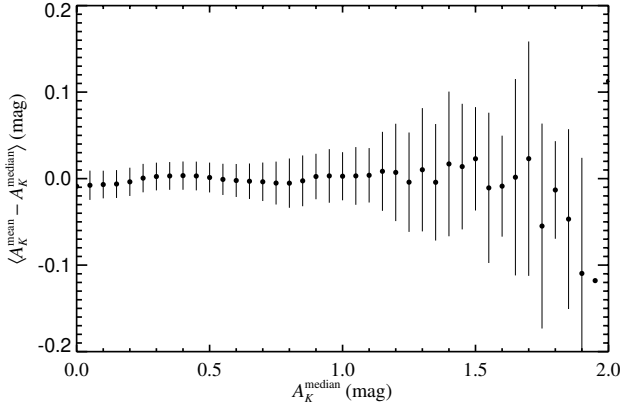
Fig. 17. This plot, similarly to Fig. 16, shows the relationship between the pixel column densities measured using the median and the simple average. The plot has been produced by splitting the pixels in bins of 0.05 mag in A_K^{median}, and by plotting, for each bin, the average and the 2-σ scatter of the quantity $A_K^{\mathrm{mean}} - A_K^{\mathrm{median}}$.
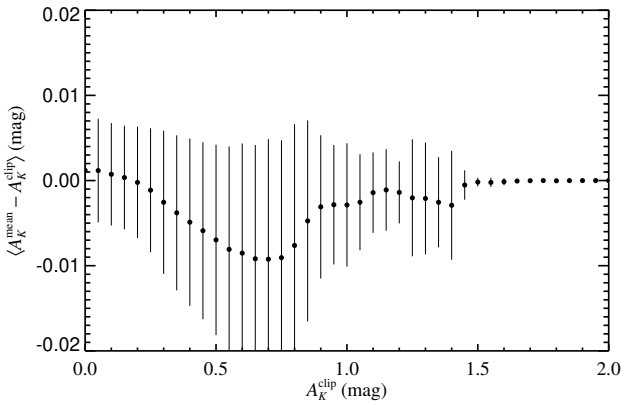
Fig. 18. This figure compares the column densities obtained through sigma-clipping and simple average, similarly to what done in Fig. 17 for the median.

A statistical comparison between the simple mean and the σ-clipping smoothing techniques is shown in Fig. 18. From this figure, we can deduce that there is no significant difference in using these two techniques. This is mostly due to the fact that the two methods are expected to provide different results only at high A_K, when a possibly significant number of foreground stars might contaminate the map. On the other hand, these regions also have a much smaller star density, and thus the extinction map there will have a large error (see Fig. 8). This, in turn, implies that the sigma clipping is not effective there (the statistical error on the map is large enough to accommodate, within a 3-σ interval, unreddened stars). Hence, in the following we will only consider the median and the simple mean estimator.

In conclusion, our analysis shows that the simple mean estimator, which has the smallest scatter, is reliable up to approximately $A_K \simeq 1.5$ mag; for larger column densities, the median should be used in order to minimize the effect of foreground stars.

4.4. Foreground star contamination

The three smoothing methods described above differ significantly on the effect of foreground contamination. If we assume that a fraction $F > 0$ of stars are foreground with respect to the cloud, then the simple average estimate will be biased toward small column densities. In particular, the average measurement of A_K will be $\langle \hat{A}_K \rangle = (1 - F) A_K^{\mathrm{true}}$. In contrast, the median will provide an (almost) unbiased estimate of A_K as long as $F < 0.5$ (see Cambrésy et al. 2002; and Lombardi 2005, for a detailed discussion of the median properties). The sigma-clipping estimate will often be between these two extremes: it will be effective in removing foreground stars only in relatively dense regions and only for small values of F.

Because of selection effects, the value of F changes significantly on the field, and in particular increases in high-column density regions. This, in turn, implies that the correction to be used on the estimated value of A_K is not constant on the field. In the case of the Pipe nebula only a few magnitude extinction in V is observed in most of the field (see above Sect. 2; see also Fig. 27 below), and thus the value of F is expected to be approximately constant. Moreover, since this cloud complex is very close to us and is observed close to the galactic center, we expect only a tiny fraction of foreground stars.

In order to evaluate quantitatively the density of foreground stars, we have selected high-extinction regions characterized by $A_K > 0.8$ mag and with relatively small expected error in A_K (we allowed for a maximum error of 0.2 mag). In order to avoid the effects of possible substructures and ambiguities in the identification of foreground stars, we restricted our analysis to the main core of the Pipe nebula, i.e. to the region at $l \simeq 1.5°$ and $b \simeq 4°$ (see Fig. 7). We have then checked all stars in these regions that show "anomalous" extinction, i.e. stars whose column densities differ by more than 3-σ with respect to the field. A total of 70 stars met this criteria; hence, since the area selected is approximately 1057 arcmin^2, we estimated a foreground star density of 0.066 arcmin^{-2}. As a result, the relative fraction of foreground stars in regions with negligible absorption is only $F|_{A_V=0} \equiv F_0 = 0.003$, and we can safely ignore the effect of foreground stars except on the higher extinction regions. Note, in particular, that a clear sign of very high extinction (very few background stars) and contamination by foreground stars is observed only in Barnard 59, where we see a "hole" in the extinction close to the center of this clump (see Fig. 19). In this case, these foreground stars are not really foreground but young stars moderately embedded in Barnard 59, an active star forming region (e.g. Onishi et al. 1999). Our estimate of F_0 allows us to evaluate the maximum theoretical extinction measurable with the NICE and NICER method: using Eq. (53) of Lombardi (2005), we obtain $A_K^{\mathrm{max}} \simeq 2.9$ mag, which is close to the maximum value measured here.

4.5. Column density distribution

A fundamental statistical property of a cloud is the distribution of column densities. Vazquez-Semadeni (1994) showed that for highly supersonic flows (such that the Mach number $M = u/c_s \gg 1$), the gas essentially has a pressureless behavior, and gravitational forces can also become negligible. In these conditions, the hydrodynamic equations become scale-invariant: in other words, motions at different length and density scales obey essentially the same equations. For a fully developed turbulent gas, density and velocity can be regarded as random fields. Because of the scale invariance, the probability of having a local (volume) density fluctuation of amplitude $\Delta\rho$ depends uniquely on the ratio $\Delta\rho/\rho$, i.e. on the *relative* fluctuation amplitude; hence, the probability distribution function of the density at each point of the cloud is expected to be lognormal. When projecting the three-dimensional mass density along the line of sight, the lognormal distribution is essentially preserved, i.e. the
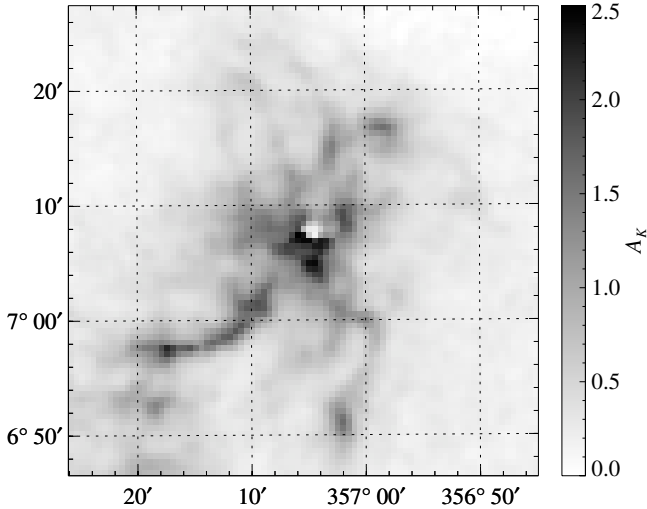
Fig. 19. A zoom of the extinction map showing Barnard 59. Note the white "hole" close to the center of this cloud, which is due to the combined effect of very high extinction values and the presence of embedded stars in this star forming core.

Table 1. The best-fit parameters obtained from a fit of the column density distribution shown in Fig. 20 using a single lognormal distribution, three lognormal distributions, or four normal distributions.

Distr.	x_0 (mag)	x_1 (mag)	σ (mag)	Rel. factor
lnGau #1	−0.241	0.503	0.325	1.000
lnGau #1	−0.150	0.413	0.501	0.150
lnGau #2	−1.805	1.943	0.018	0.744
lnGau #3	0.039	0.267	0.371	0.106
Gau #1	0.015	–	0.022	0.086
Gau #2	0.123	–	0.033	0.353
Gau #3	0.267	–	0.064	0.395
Gau #4	0.419	–	0.118	0.166

projected two-dimensional density is also expected to be well approximated by a lognormal distribution.

More recently, Vazquez-Semadeni argument has been investigated in more detail using various simulations by a number of authors (e.g. Padoan et al. 1997c,b,a; Passot & Vázquez-Semadeni 1998; Klessen 2000), and in all cases the lognormal distribution was found to be a good approximation of the (projected) cloud density. However, Scalo et al. (1998) found that, contrary to previous claims, the density probability distribution is well approximated in their simulations by an exponential law in a relatively large range of physical parameters. Recently, this argument has been challenged by Ostriker et al. (2001) by showing a good agreement with a lognormal distribution in the molecular cloud IC 5146 (Lada et al. 1999). A direct study of the extinction distribution on a real cloud is a stringent test for simulations and ultimately also provides important hints on the physical conditions inside molecular clouds. We evaluated the column density distribution in the Pipe nebula by constructing the histogram of extinction measurements in each pixels of the map shown in Fig. 7 with $b > 3°$, binned on suitable intervals (we used here 0.002 mag in A_K). The obtained distribution, plotted in Fig. 20, shows a complex shape with multiple peaks.

In order to compare the empirical distribution with a theoretical one, we used Poisson models for the individual histogram bins, and evaluated the joint probability to have the observed histogram in the range $−0.3$ mag $< A_V < 2$ mag (we excluded
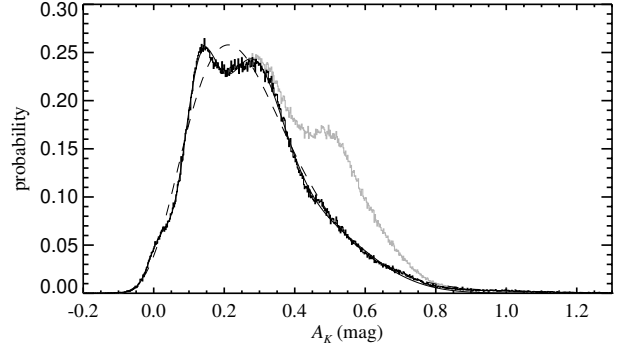
Fig. 20. The distribution of pixel extinction over the whole field. The figure shows the histogram of column densities for all pixels (gray line) and for the pixels with galactic latitude $b > 3°$. Note that the latter histogram can be fitted almost perfectly using four normal distributions (solid line) or four lognormal distributions (not shown here), while a single lognormal (dashed lined) is able to reproduce the general shape of the histogram.

high A_K bins in order to avoid the complications inherent with large-column density regions). We constructed the theoretical models as sum of normal distributions

$$\mathrm{Gau}(x|x_0, \sigma^2) = \frac{1}{\sqrt{2\pi\sigma^2}} \exp\left(-\frac{(x - x_0)^2}{2\sigma^2}\right), \quad (12)$$

and lognormal ones

$$\mathrm{lnGau}(x|x_0, x_1, \sigma) =$$
$$\frac{1}{(x - x_0)\sqrt{2\pi\sigma^2}} \exp\left(-\frac{\left[\ln(x - x_0) - \ln x_1\right]^2}{2\sigma^2}\right). \quad (13)$$

As shown by Fig. 20, the best fit obtained from a single lognormal (dashed line) is surprisingly good given the complexity of the distribution; clearly, however, in this case we are only able to reproduce the general shape of the histogram and we are unable to generate finer details clearly visible in Fig. 20. As a measure of the quality of the fit, we note that the residuals are more than 150σ away from the observed histogram.

In order to improve the fit we added more components. However, two-component distributions still gave unsatisfactory results, and we had to use more components distributions to obtain a close match to the data. In particular, we verified that both the sum of four normal and three lognormal distributions gave similar fits, with residuals of the order of 8σ. Hence although, in principle, the fit is still statistically inconsistent with the data, we note that in practice the large number of bins and the non-trivial structure of the Pipe nebula make it difficult to obtain good fits with a relatively small number of parameters. Note also that the need for several components in the column-density distribution is reminiscent of the velocity structures observed in the Pipe nebula from CO data (Onishi et al. 1999). In this respect, it is also likely that some of the "weak" components (e.g., the lnGau #3 or the Gau #4) are related to background clouds observed in projection to the Pipe nebula at low galactic latitudes.

5. Comparison with CO analysis

Radio observations of H_2 surrogates, and in particular of CO isotopes, provide an alternative independent estimate of the cloud gas column density. Onishi et al. (1999) studied in detail the Pipe nebula with the NANTEN radiotelescope and kindly provided
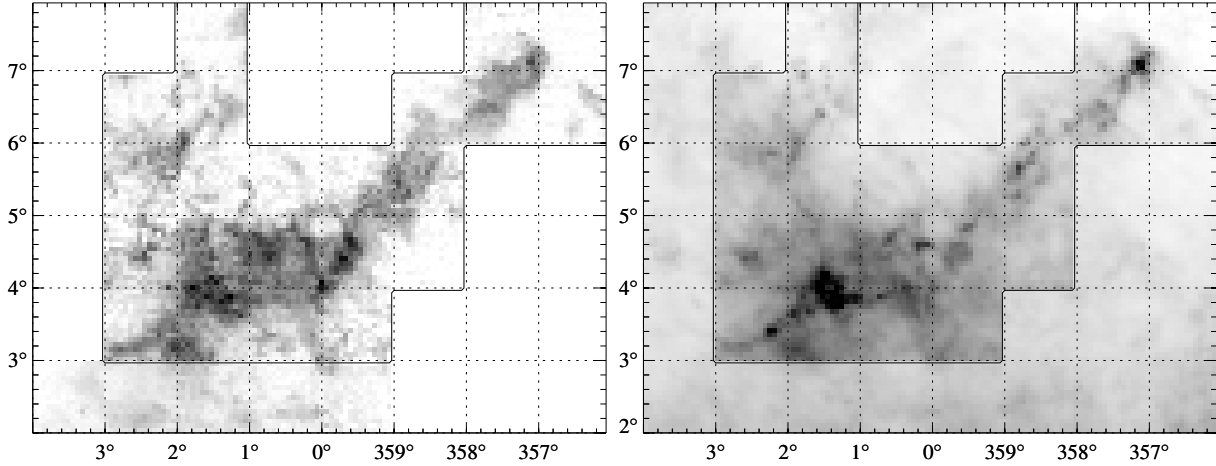
Fig. 21. *Left*: the NANTEN integrated ^{12}CO column density map (kindly provided by Onishi et al. 1999); the white regions have not been observed and no data are thus available there; the shaded region is located at $b < 3°$ and has been excluded from the analysis to avoid contamination from low-galactic latitude clouds. *Right*: the NICER extinction map downgraded to the resolution of the NANTEN map; shaded regions are excluded from the analysis.
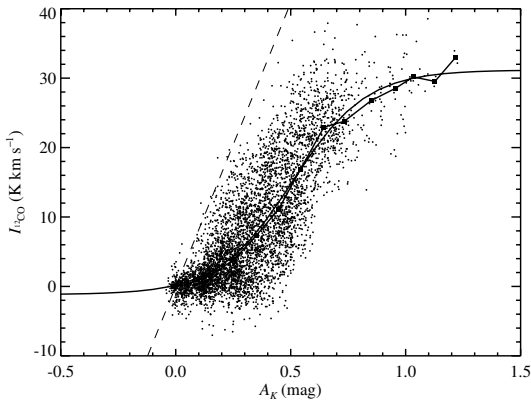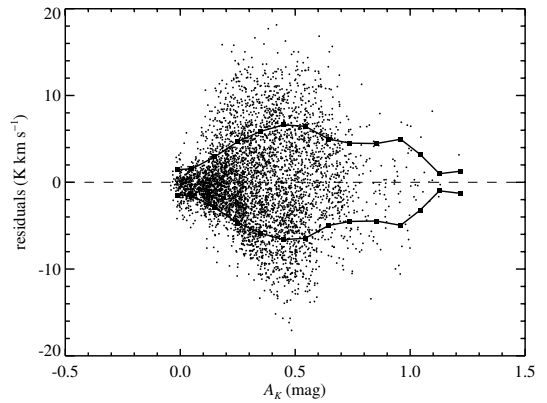

Fig. 22. The ^{12}CO integrated intensity I_{12CO} as a function of the NICER extinction. Each point of this plot shows the ^{12}CO radio measurement from Onishi et al. (1999) and the NICER extinction at the corresponding position. The filled squares represent the average ^{12}CO intensity in bins of 0.1 mag of K-band extinction; the solid, smooth line is the best fit for functions of the form of Eq. (14); the dashed line shows the linear relation used by Onishi et al. (1999) (X-factor 2.8×10^{20} cm^{-2} K^{-1} km^{-1} s).

Fig. 23. The residuals in the best-fit (14) of Fig. 22. The filled squares represent the standard deviations in bins of 0.1 mag.

their ^{12}CO map to perform a comparison with the NICER analysis described in this paper. To this purpose, we constructed an extinction map using the same resolution (4 arcmin) and coordinate system of the NANTEN observations. In order to avoid any contamination by low-galactic latitude clouds, we excluded all measurements at $b < 3°$ (see Fig. 21).

Figure 22 shows the relationship between the NICER column density and the NANTEN integrated ^{12}CO temperature, $I_{12CO} \equiv \int T \, dv$. The large number of independent measurements shown in this figure ($\sim$5000) was used to compare these two estimates of the gas column density and to show the limits and merits of both.

From Fig. 22 we can deduce a number of qualitative points. We first note that apparently ^{12}CO measurements are insensitive to low column density regions. Specifically, it appears that up to $\sim$0.2 mag of K-band extinction the radio measurements are uniformly distributed around 0 K km s^{-1}. The relatively small scatter observed in Fig. 22 up to 0.15−0.2 mag of extinction (cf. also Fig. 23) indicates that both methods considered here have small intrinsic internal errors.

At higher extinctions, and up to $A_K \simeq 0.6$ mag, we observe an almost linear relationship between the extinction and the ^{12}CO measurements; correspondingly, the scatter in the plot increases significantly (see below). We note that the presence of a linear relationship between the CO integrated temperature and the NIR extinction (and thus the hydrogen projected density), although on a relatively small extinction range, is not obvious on the scales considered here and for non-virialized cloud systems (see Dickman et al. 1986). Finally, for $A_K \gtrsim 0.7$ mag, the ^{12}CO data appear to saturate to a constant value close to 30 K km s^{-1}. This well-known saturation effect is described in terms of an exponential relation between the integrated temperature $I_{12CO} \propto 1 - e^{-\tau}$ and the cloud optical depth $\tau \propto A_K$. The following analysis will mostly focus on the unsaturated ^{12}CO regime and will thus directly make use of the integrated temperature.

A more quantitative analysis of Fig. 22 was carried out as follows. We divided the measurements in regular bins in A_K (we used a bin size of 0.1 mag), and we computed in each bin the average of the ^{12}CO intensity. The results obtained are shown as filled squares in Fig. 22. This simple plot confirmed the qualitative remarks discussed above and suggested that we could approximate the $A_V - ^{12}$CO relationship with a function of the form

$$I_{12CO} = A \left[\frac{1}{1 + \exp\left[-(A_K - A_K^{\text{mid}})k\right]} - b \right]. \tag{14}$$
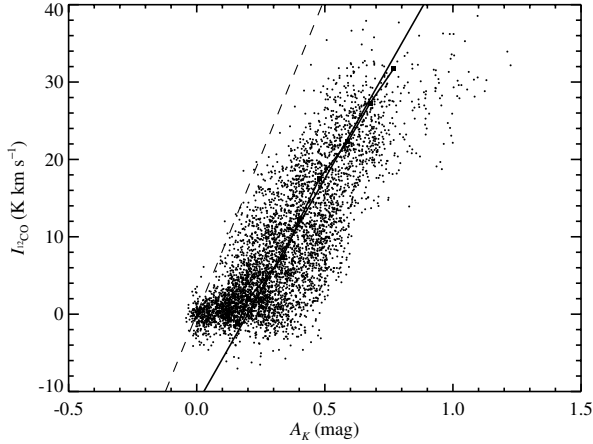
Fig. 24. The ^{12}CO–A_K relation, with datapoints binned along the CO axis every 5 K km s^{-1} (filled squares). The solid line represents the best fit (on the whole field) from Eq. (15).

We fitted this equation to the data by minimizing the scatters between the predicted CO integrated intensity and the observed one; the best fit parameters obtained were $A = 32.3$ K km s^{-1}, $A_K^{\text{mid}} = 0.51$ mag, $k = 6.20$ K km s^{-1} mag^{-1}, and $b = 0.036$. The residuals of this fit with the data are shown in details in Fig. 23; the increase of the dispersion in the relation (14) at $A_K \simeq 0.2$ mag is evident from this plot. Since the expected error in the NICER map of Fig. 21 is as low as ~0.01 mag, and since the expected error in the ^{12}CO integrated velocities is also relatively small (this can be estimated from the residuals at $A_K \simeq 0$ mag of Fig. 23, and is of order of 1.5 K km s^{-1}), we can deduce that the scatter shown in Fig. 23 for $A_K > 0.2$ mag is physical: the ratio of dust and ^{12}CO in the Pipe (and likely in other molecular clouds) is far from being constant.

So far we investigated the A_K–^{12}CO relationship using the value of A_K as independent quantity: in other words, we studied the expected CO measurement for each given A_K column density. We now swap the role of A_K and CO, and consider the average A_K value corresponding to a given ^{12}CO measurement. To this purpose, we averaged the values of the NICER extinction in bins of 5 K km s^{-1}. The result, shown in Fig. 24, suggests that we can well approximate the average with a linear relationship of the form

$$A_K = A_K^{(0)} + rI_{^{12}\text{CO}}. \tag{15}$$

Note that we need to include explicitly a non-vanishing "zero point", $A_K^{(0)}$, for the A_K measurement. This is due the dissociation of the CO molecule by the interstellar UV radiation field. Our results indicate that CO molecules in the Pipe become (self-) shielded from the interstellar radiation field at about 1 mag of visual extinction (2 mag along the entire line of sight through the cloud), consistent with standard theoretical predictions and prior observations (e.g., van Dishoeck & Black 1988; Alves et al. 1999; Bergin et al. 2002). This CO threshold should in principle be a function of the intensity of the local interstellar radiation field and could in principle vary from cloud to cloud. We stress that it is highly unlikely that the NICER technique overestimates the extinction at low A_K, i.e. that the "zero point" observed in the relation (15) is an artifact; rather, if there is a bias in NICER, this is likely to be toward an *underestimate* of the column density (because of a possible reddened control field).

Our data, combined with the ^{12}CO data, allows for the best determination of the CO-to-H$_2$ conversion factor (X-factor) using dust as a tracer of H$_2$, because of the large number of measurements (approximately 5000) and also because our

Table 2. Best fit parameters relative to Eq. (15). If a normal reddening law is assumed, the X-factors derived from these fits are $\{4.21, 3.93, 3.77, 2.91\} \times 10^{20}$ cm^{-2} K^{-1} km^{-1} s respectively. The formal, 1σ errors are 0.002 mag and 0.0002 for $A_K^{(0)}$ and r, respectively (for all four fits).

| Fit	$A_K^{(0)}$ (mag)	r (mag K^{-1} km^{-1} s)
Whole sample	0.176	0.0184
$I_{^{12}\text{CO}} > 5$ K km s^{-1}	0.199	0.0172
$A_K > 0.1$ mag	0.211	0.0165
$A_K \in [0.1, 0.6]$ mag	0.226	0.0127
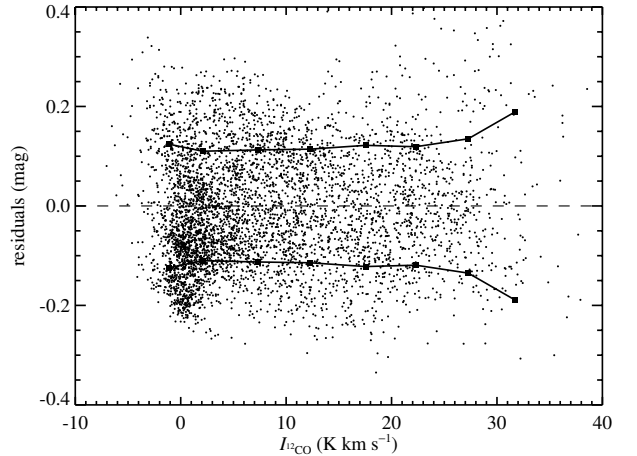
Fig. 25. The scatter of our measurements on the linear fit of Eq. (15). Note how the derived standard deviation (filled squares) is practically constant over the CO column densities investigated here.

(smoothed) dust extinction measurements have a mean error smaller than 0.05 mag of visual extinction. To derive the X-factor for the ^{12}CO data we performed several best fits using Eq. (15) using different selections of the points of Fig. 24; the results obtained are reported in Table 2.

Finally, Fig. 25 shows the residuals obtained from the fit of Eq. (15). Interestingly, these residuals appear to be rather constant on the field, and their standard deviation is approximately 0.1 mag in K-band extinction (or about 1 mag of visual extinction): hence, a single pointing in ^{12}CO can only constrain the dust column density with an accuracy of a few magnitudes. Remarkably, this result is consistent with that found by Lada et al. (1994) for ^{13}CO in the molecular cloud IC 5146, Alves et al. (1999) for ^{18}CO in L977, and Bergin et al. (2002) for the molecular cloud Barnard 68. Hence, we find what it seems to be an irreducible uncertainty in the dust-CO correlation of about 1 mag of visual extinction. The cause for this irreducible uncertainty is not known and it deserves a dedicated study. A possible origin for this uncertainty might lie in the sensitivity of the CO molecule (and its isotopes) to variations in temperature (even along the same line-of-sight), density and UV radiation field (e.g. Frerking et al. 1982; van Dishoeck & Black 1988). We note however that changes in the abundance of ^{12}CO, due to freezing out on grains, are probably not in place at the extinctions less than $A_K \simeq 1$ mag considered here when comparing the NANTEN and 2MASS/NICER analyses.

In order to further test this point, we considered the difference between the NICER extinction and the ^{12}CO integrated intensity. In particular, we converted the degraded A_K NICER extinction map shown in Fig. 21 (right) into a ^{12}CO intensity using Eq. (14), and subtracted from this map the NANTEN ^{12}CO extinction map. The result obtained, shown in Fig. 26, gives
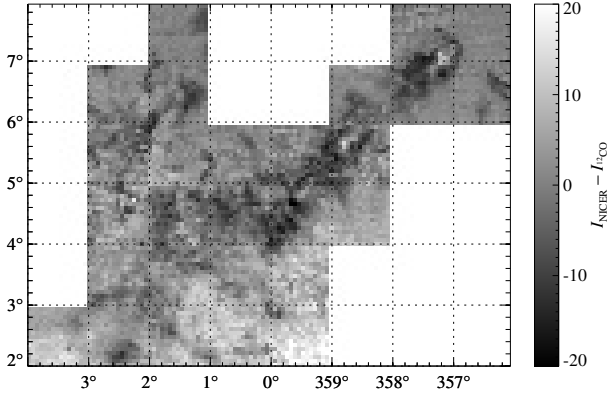
Fig. 26. The difference between the two maps of Fig. 21, i.e. the NICER extinction map, converted into intensity using Eq. (14), and the ^{12}CO intensity.

insight into the origin of the scatter observed in Fig. 22. The first striking fact is that clear structures are observed in Fig. 26, and this alone rules out the possibility that the difference between the 2MASS-NICER and the NANTEN measurements is due to statistical errors. Instead, in large areas we observe systematically positive or negative values of the difference between the two maps.

In analysing Fig. 26 one should always keep in mind that this map has been built by converting the NICER column density into a radio intensity by using the best fit provided by Eq. (14); hence, differences have to be interpreted as deviations from the fit used. With this point in mind, we can deduce some interesting facts from Fig. 26:

- The outer regions of the nebula appear to have consistent measurements in radio and NIR. Given the form of Eq. (14), this further confirms that ^{12}CO observations are insensitive to low column densities.
- In many peripheral parts of the Pipe nebula, the ^{12}CO intensity appears to overestimate the (converted) NICER column density (see, e.g., the dark region in the middle of Fig. 26). This effect, in principle, could be related to differences in the photo-dissociation of CO molecules due to variations of the local interstellar radiations field. However, since generally an *excess* of ^{12}CO intensity is observed in the *periphery* of the Pipe, it is more likely that the effect is related to temperature gradients in the nebula (this is also suggested by the patchy aspect of the map of Fig. 26).
- The dense cores (e.g., Barnard 59) generally appear bright in Fig. 26, indicating that the ^{12}CO map underestimates the column density there when compared to the NICER analysis. This effect is clearly due to the saturation effect of ^{12}CO at high column densities (the saturation hence appears to be even stronger than suggested by Fig. 22 and by the fit (14)).

The items above proves that a joint analysis of the NICER and CO results can provide nontrivial and interesting insights into the structure of molecular clouds and the process that regulate the radio emission. Clearly, the results obtained here are specific to the Pipe nebula; however, by carrying out similar discussions for other cloud complexes we hope to be able to draw general conclusions on this important topic.

6. Mass estimate

The cloud mass M can be derived from the A_K extinction map using the following simple relation

$$M = d^2 \mu \beta_K \int_\Omega A_K \, d^2 x, \qquad (16)$$

where $d = 130$ pc is the cloud distance, μ is the mean molecular weight corrected for the helium abundance, $\beta_K \simeq 1.67 \times 10^{22}$ cm^{-2} mag^{-1} is the ratio $N(\text{HI}) + N(\text{H}_2)/A_K$ (Savage & Mathis 1979; see also Lilley 1955; Bohlin et al. 1978), and the integral is evaluated over the whole field Ω. Assuming a standard cloud composition (63% hydrogen, 36% helium, and 1% dust), we find $\mu = 1.37$ and a total mass $M = (11\,000 \pm 2600)\, M_\odot$. The error is mainly due to the uncertainty on the distance of the cloud. Note that in this analysis we only included measurements above $b > +3°$ (see discussion above in Sect. 2).

Our mass estimate apparently compares well with the independent one of Onishi et al. (1999), $M \simeq 10^4\, M_\odot$. Note, however, that if we use the cloud distance assumed by Onishi et al. (1999), $d = 160$ pc, we obtain a larger mass, $M = 1.7 \times 10^4\, M_\odot$, i.e., the CO derived mass is only about 65% the dust derived mass. As discussed in Sect. 5, this discrepancy can in principle be attributed to (1) the insensitivity of ^{12}CO to low column densities; (2) to the saturation of ^{12}CO in the dense cores of the cloud; and (3) to a relatively small X-factor used by Onishi et al. (1999). We can rule out the latter as the X-factor used by Onishi et al. (1999) (2.8×10^{20} cm^{-2} K^{-1} km^{-1} s) is virtually coincident (96%) with the one derived in this paper (2.91×10^{20} cm^{-2} K^{-1} km^{-1} s).

To investigate the source of discrepancy in the mass estimates we present in Fig. 27 the relationship between the integrated mass distribution and the extinction in A_K. We also plot, as a dashed line, the smoothed and clipped extinction map that was compared to the CO data (see Fig. 21). Note that regions with extinction larger than $A_K > 0.6$ magnitudes (where the CO-dust correlation breaks at higher column densities) account for about 20% of the total mass (dashed line). Similarly, note how regions with $A_K < 0.25$ mag, the column density threshold below which CO is not sensitive to H_2, account for about 15% of the cloud mass. The total fraction of dust mass that is missed by the CO is then about 35%, which, within the approximations, solves the discrepancy found between the dust and CO derived mass.

7. Conclusions

The main results of this paper can be summarized as follows:

- We used 4.5 million stars from the 2MASS point source catalog to construct a $8° \times 6°$ extinction map of the poorly studied Pipe nebula, a molecular cloud complex seen in projection towards the galactic bulge. The map has a resolution of 1 arcmin and has a 3σ detection level of 0.5 visual magnitudes.
- We combined the 2MASS data with Tycho and Hipparcos parallaxes to obtain a distance of 130 ± 15 pc to this molecular complex. We estimated, for this distance, a total mass of $\sim 10^4\, M_\odot$ for the Pipe complex. This makes the Pipe nebula one the closest star forming region to the Earth of its type, closer than the Ophiuchus and the Taurus complexes.
- We studied in details the statistical properties of the extinction map obtained through the NICER method. We also confirmed the relation originally observed by Lada et al. (1994) for IC 5146, suggesting that there is unresolved structure at the highest extinctions in our map.
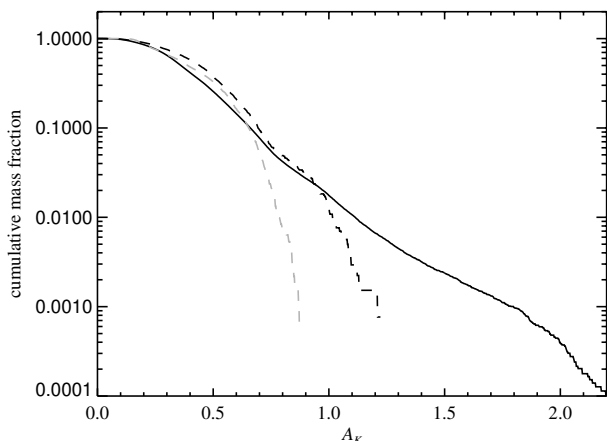
Fig. 27. The cumulative mass enclosed in isoextinction contours. The plot has been constructed using only extinction measurements at galactic latitude $b > 3°$ (cf. Fig. 20). The solid line shows the cumulative mass from the whole NICER map, the dashed black line the cumulative mass from the downgraded (and clipped) map of Fig. 21 right, and the dashed grey line the cumulative mass derived from the NANTEN observations (see Fig. 21 right). For this latter mass estimate we used the conversion formula (15).

- We compared our near-infrared study with the CO observations of Onishi et al. (1999), and derived fitting formulae to relate the ^{12}CO column density with the A_K extinction. We also derived the dust-to-^{12}CO ratio, and showed that if a normal infrared reddening law is assumed, then the derived X-factor is as large as 2.91×10^{20} cm^{-2} K^{-1} km^{-1} s in the range $A_K \in [0.1, 0.6]$ mag.

- We found that ^{12}CO is only sensitive to about 65% of the total dust mass. About half of the missing mass is not traced by CO at column densities below $A_K < 0.25$ mag, and half is not traced at column densities above $A_K > 0.6$ mag, where the line begins to saturate. There is an apparently irreducible uncertainty in the dust-CO correlation of about 1 mag of visual extinction. This uncertainty seems to be independent of the cloud or the interstellar radiation field.

- We took advantage of the large number of background sources to accurately measure the NIR reddening law for this cloud, and obtained $E(J − H) = (1.85 ± 0.15)E(H − K)$, in very good agreement with the standard Rieke & Lebofsky (1985) reddening law.

- Finally from analysis of the JHK color−color diagram for the Pipe region we identify a large population of red stars whose colors are distinct from those of typical reddened background giants. These stars are spatially distributed over the entire observed field, preferentially located at lower Galactic latitudes and are not associated with the molecular cloud. These stars are the brightest stars detected in the field and have a very narrow distribution in magnitude space. These properties are similar to those of Galactic OH/IR stars. Our observations thus appear to have provided one of the largest samples of such stars yet discovered.

References

Alves, J., Lada, C. J., Lada, E. A., Kenyon, S. J., & Phelps, R. 1998, ApJ, 506, 292
Alves, J., Lada, C. J., & Lada, E. A. 1999, ApJ, 515, 265
Alves, J., Lada, C. J., & Lada, E. A. 2001, Nature, 409, 159
Alves, J., Lada, C., Lada, E., Lombardi, M., & Bergin, E. A. 2002, in The Origins of Stars and Planets: The VLT View, Proc. of the ESO Workshop held in Garching, Germany, 24−27 April 2001, 37
Andre, P., Ward-Thompson, D., & Barsony, M. 2000, in Protostars and Planets IV (Book – Tucson: University of Arizona Press), ed. V. Mannings, A. P. Boss, & S. S. Russell, 59
Bahcall, J. N., & Soneira, R. M. 1980, ApJS, 44, 73
Bergin, E. A., Ciardi, D. R., Lada, C. J., Alves, J., & Lada, E. A. 2001, ApJ, 557, 209
Bergin, E. A., Alves, J., Huard, T., & Lada, C. J. 2002, ApJ, 570, L101
Bianchi, S., Gonçalves, J., Albrecht, M., et al. 2003, A&A, 399, L43
Blitz, L., & Williams, J. P. 1999, in The Origin of Stars and Planetary Systems, NATO ASIC Proc., 540, 3
Bohlin, R. C., Savage, B. D., & Drake, J. F. 1978, ApJ, 224, 132
Cambrésy, L., Beichman, C. A., Jarrett, T. H., & Cutri, R. M. 2002, AJ, 123, 2559
Carpenter, J. M. 2001, AJ, 121, 2851
Chini, R. 1981, A&A, 99, 346
Dickman, R. L., Snell, R. L., & Schloerb, F. P. 1986, ApJ, 309, 326
Frerking, M. A., Langer, W. D., & Wilson, R. W. 1982, ApJ, 262, 590
Heyer, M. H., Brunt, C., Snell, R. L., et al. 1998, ApJS, 115, 241
Indebetouw, R., Mathis, J. S., Babler, B. L., et al. 2005, ApJ, 619, 931
Jiménez-Esteban, F. M., Agudo-Mérida, L., Engels, D., & García-Lario, P. 2005, A&A, 431, 779
Johnstone, D., Wilson, C. D., Moriarty-Schieven, G., et al. 2000, ApJ, 545, 327
Kenyon, S. J., Lada, E. A., & Barsony, M. 1998, AJ, 115, 252
Kharchenko, N. V. 2001, Kinematika i Fizika Nebesnykh Tel, 17, 409
Kleinmann, S. G., Lysaght, M. G., Pughe, W. L., et al. 1994, Exp. Astron., 3, 65
Klessen, R. S. 2000, ApJ, 535, 869
Knude, J., & Hog, E. 1998, A&A, 338, 897
Koresko, C. D. 2002, AJ, 124, 1082
Kramer, C., Alves, J., Lada, C., et al. 1998, A&A, 329, L33
Kramer, C., Alves, J., Lada, C. J., et al. 1999, A&A, 342, 257
Kramer, C., Richer, J., Mookerjea, B., Alves, J., & Lada, C. 2003, A&A, 399, 1073
Lada, C. J., Lada, E. A., Clemens, D. P., & Bally, J. 1994, ApJ, 429, 694
Lada, C. J., Alves, J., & Lada, E. A. 1999, ApJ, 512, 250
Lada, C. J., Bergin, E. A., Alves, J. F., & Huard, T. L. 2003, ApJ, 586, 286
Lada, C. J., Huard, T. L., Crews, L. J., & Alves, J. F. 2004, ApJ, 610, 303
Lallement, R., Welsh, B. Y., Vergely, J. L., Crifo, F., & Sfeir, D. 2003, A&A, 411, 447
Landolt-Börnstein 1982, Numerical Data and Functional Relationships in Science and Technology, Vol. 2B, Stars and star clusters (Berlin: Springer-Verlag), 15
Lilley, A. E. 1955, ApJ, 121, 559
Lindegren, L., & Perryman, M. A. C. 1996, A&AS, 116, 579
Lombardi, M. 2005, A&A, 438, 169
Lombardi, M., & Alves, J. 2001, A&A, 377, 1023
Myers, P. C. 1999, in The Origin of Stars and Planetary Systems, NATO ASIC Proc., 540, 67
Onishi, T., Kawamura, A., Abe, R., et al. 1999, PASJ, 51, 871
Ostriker, E. C., Stone, J. M., & Gammie, C. F. 2001, ApJ, 546, 980
Padoan, P., Jimenez, R., & Antonuccio-Delogu, V. 1997a, ApJ, 481, L27
Padoan, P., Jimenez, R., & Jones, B. 1997b, MNRAS, 285, 711
Padoan, P., Jones, B. J. T., & Nordlund, A. P. 1997c, ApJ, 474, 730
Passot, T. & Vázquez-Semadeni, E. 1998, Phys. Rev. E, 58, 4501
Perryman, M. A. C., Lindegren, L., Kovalevsky, J., et al. 1997, A&A, 323, L49
Reipurth, B., & Zinnecker, H. 1993, A&A, 278, 81
Reipurth, B., Nyman, L.-A., & Chini, R. 1996, A&A, 314, 258
Rieke, G. H., & Lebofsky, M. J. 1985, ApJ, 288, 618
Savage, B. D., & Mathis, J. S. 1979, ARA&A, 17, 73
Scalo, J., Vazquez-Semadeni, E., Chappell, D., & Passot, T. 1998, ApJ, 504, 835
Simon, R., Jackson, J. M., Clemens, D. P., Bania, T. M., & Heyer, M. H. 2001, ApJ, 551, 747
Tanner, M. 1991, Tools for Statistical Inference, lecture notes in statistics (Berlin: Springer-Verlag), 67
van Dishoeck, E. F., & Black, J. H. 1988, ApJ, 334, 771
Vazquez-Semadeni, E. 1994, ApJ, 423, 681
Wainscoat, R. J., Cohen, M., Volk, K., Walker, H. J., & Schwartz, D. E. 1992, ApJS, 83, 111
Wright, C. O., Egan, M. P., Kraemer, K. E., & Price, S. D. 2003, AJ, 125, 359